Physical issues in shock ignition

D. Batani[1], S. Baton[2], A. Casner[3], S. Depierreux[3], M. Hohenberger[4], O. Klimo[5], M. Koenig[2], C. Labaune[2], X. Ribeyre[1], C. Rousseaux[3], G. Schurtz[1], W. Theobald[4], V. T. Tikhonchuk[1]

[1] University Bordeaux - CNRS - CEA, Centre Lasers Intenses et Applications, UMR 5107, 33405 Talence, France
[2] LULI, CNRS - CEA - École Polytechnique - UPMC, 91128 Palaiseau, France
[3] CEA, DAM, DIF, F-91297 Arpajon, France
[4] Laboratory for Laser Energetics, University of Rochester, Rochester, NY 14623, USA
[5] Czech Technical University in Prague, FNSPE, 11519, Prague, Czech Republic

E-mail: tikhonchuk@celia.u-bordeaux1.fr

Abstract. The paper presents theoretical analysis and experimental results concerning the major physical issues in the shock ignition approach. These are: generation of a high amplitude shock in the imploding target, laser-plasma interaction physics in the conditions of high laser intensities needed for high amplitude shock excitation, symmetry and stability of the shock propagation, role of fast electrons in the symmetrization of the shock pressure and the fuel preheat. The theoretical models and numerical simulations are compared with the results of specially designed experiments on laser plasma interaction and shock excitation in plane and spherical geometries.

PACS numbers: 52.57.Kk, 52.38.-r, 52.50.Jm

Submitted to: *Nuclear Fusion*

1. Introduction

Shock ignition is a relatively new scenario in inertial confinement fusion. The initial idea by Shcherbakov [1] has been rediscovered by Betti and co-authors [2] and applied to the target design in Refs. [3, 4, 5, 6]. A more detailed review of the shock ignition scheme is presented in the accompanying paper [7]. The attractiveness of shock ignition scheme relies first of all on a relatively simple and robust implosion scheme and the ignition scheme that can be realized on the existing laser installations. The implosion implies a rather conservative laser temporal profile with the intensities of the order of a few hundred TW/cm^2 where the laser plasma interactions proceed essentially in a classical collisional regime, which is well-known theoretically and is confirmed in many experiments. The laser radiation is absorbed in a plasma corona, most efficiently near the critical density where the laser frequency is equal to the electron plasma frequency. The absorbed energy is transported to high densities with the heat flux of thermal electrons where it creates ablation, and the pressure of ablated vapors push forward the solid shell. The shell acceleration and implosion velocity are significantly lower than in the common central ignition scheme. In combination with a longer laser pulse the shell implosion is expected to be more stable providing access to relatively large fuel areal densities at laser pulse energies of a few hundred kJ. However a hot spot temperature in a keV range is insufficient for self-ignition.

The ignition is achieved with a strong shock which is launched at the end of implosion phase by raising abruptly the laser intensity by one or two orders of magnitude. Laser plasma interactions at this stage are strongly nonlinear and are not sufficiently investigated experimentally at the moment, but it is expected that the quality of absorption would be sufficient to create the required ablation pressure. The physics of laser spike absorption and ablation pressure enhancement are the major unknowns in the shock ignition scenario. These issues will be discussed in the present paper.

The ablation pressure $p_{\rm abl}$ in the regime of classical collisional absorption is proportional to the laser intensity and the critical density. In the quasi-stationary regime of laser plasma interaction it is described by the following scaling law [8, 9, 10]

$$p_{\rm abl} \approx 57\,(\eta_{\rm abs} I_{\rm PW}/\lambda_{\mu\rm m})^{2/3}\,\text{Mbar}, \tag{1}$$

where $\eta_{\rm abs}$ is the laser absorption coefficient, $I_{\rm PW}$ is the laser intensity in units of PW/cm^2 and $\lambda_{\mu\rm m}$ is the laser wavelength in microns. For $\lambda = 0.35\,\mu$m, $I = 0.3\,$PW/cm^2 and $\eta_{\rm abs} \simeq 0.7$, the ablation pressure at the implosion stage is about 40 Mbar leading to a relatively slow and hydrodynamically-stable implosion at velocities of the order of 250 km/s (or 250 μm/ns). It creates a central hot spot with parameters somewhat below the ignition curve. Ignition is boosted with a specially designed *ignition shock* that is launched just before the stagnation. It should have a rather high amplitude of the order of 300 Mbar to bring to the hot spot an entropy necessary for ignition. According to (1), the corresponding laser intensity exceeds 5 PW/cm^2 (assuming $\lambda = 0.35\,\mu$m and $\eta_{\rm abs} \simeq 0.6$), and the laser power needed for the ignition shock launch is at the level of $200 - 400$ TW, which is within the operational domain of the existing laser installations – National Ignition Facility (NIF) [11] and Laser MegaJoule (LMJ) [12]. Because of lower energy invested in fuel assembly compared to the direct drive scenario, shock ignition promises higher energy gain of the order of 100 or more, which is the crucial point for a future power plant.

The fact that the laser parameters requested for shock ignition are available today makes it much different from other alternative schemes discussed in this issue, which

require for their demonstration construction of new installations with an operational power that exceeds many petawatts and with an energy of the order of hundred kilojoules. That is by itself a formidable engineering challenge. However, the plasma and laser parameters needed for the ignition shock are in a "dangerous" zone where the nonlinear effects in laser plasma interaction manifest themselves in enhanced scattering and generation of energetic electrons. The laser intensities above $1\,\mathrm{PW/cm^2}$ demonstrate increasing reflectivity levels [13] related to the stimulated Raman (SRS) and Brillouin (SBS) scattering, laser beam filamentation (FI), two plasmon instability (TPD) and other parametric processes. All these effects are not included in standard versions of hydrodynamic codes and thus may be easily underestimated. Moreover, this range of laser intensities was not studied experimentally as all other ignition schemes considered previously avoided it. Since the experiments around 1980 and later demonstrated an increasing level of SRS that is correlated with production of high energy electrons [14], no other results in this parameter domain have been reported many years.

However, the specificities of shock ignition scheme may allow one to mitigate undesirable nonlinear effects and even benefit from their presence. In difference from the standard implosion schemes, the shock ignition target is accelerated for a longer time at lower intensities, so that, at the moment of intense ignition spike arrival the shell radius is reduced by a factor of two. It is already compressed and its areal density is increased by a factor of ten or twenty approaching a level of about $10\,\mathrm{mg/cm^2}$. This value is comparable with the range of 100 keV electrons [15]. For this reason the electrons generated in the corona with lower energies may not present a danger for the hot spot preheat. They may be even beneficial when propagating to the solid shell and smoothing the inhomogeneities of the laser intensity in corona and increase the ablation pressure while depositing their energy at the outer shell surface. Moreover, at the moment of laser spike arrival the corona has a larger scale and a higher temperature. This changes considerably the conditions of excitation of parametric instabilities and their competition. As it will be shown in this paper, the recent numerical simulations and some experiments are showing the laser absorption coefficient in the range of laser intensities interesting for shock ignition remains at the acceptable level of $\eta_{\mathrm{abs}} \simeq 60-70\%$. As laser intensity increases, more absorbed energy is transported by hot electrons, but their average energy remains at the acceptable level of $30-50\,\mathrm{keV}$.

Importance of issues related to the laser plasma interaction and fast electron transport in the context of shock ignition has been recognized a few years ago and were studied analytically, numerically and experimentally. Many problems are not yet resolved, but a significant progress has been made that shows promising features of the shock ignition approach. A brief summary of these studies is presented in this review. Three major questions are addressed first theoretically and then experimentally:

- What are the specificities of laser plasma interaction in the conditions of shock ignition? What is the role of collisional processes and parametric instabilities and how do they compete? What are the characteristics of hot electrons generated in the corona? What are their energy and number and how do they transport their energy into the dense plasma? Although the interaction physics is rather complicated, the responses to these questions are encouraging indicating good absorption and relatively low hot electron energies seen in numerical simulations and in experiments.

- How is the ignition shock generated in the target and what laser intensities are needed to achieve the pressures required for ignition? How are the collisional and collective effects in the hot electron transport competing and what would be the optimal conditions for the shock launch? The possibility of generation of the shock pressures above 100 Mbar is not yet demonstrated experimentally, while the theory and simulations provide positive estimates if the hot electron transport is taken into account.
- How does the electron transport affect the symmetry of the implosion? Because of a sufficiently large distance between the zone of electron generation and the ablation surface, hot electrons may smooth out small scale inhomogeneities thus improving the shell stability and suppressing the fuel mix with the hot spot material at the internal surface of the shell. Moreover, it might be that the hot electron generation need not to be very symmetric. Thus a relatively small number of laser beams may be needed for driving the shock. This would agree rather well with the polar irradiation geometry of NIF and LMJ designed for indirect drive ignition.

Direct drive ignition experiments on these installations will be rather complicated because of the necessity of repointing and refocusing laser beams in order to equilibrate irradiation over the spherical target surface. The Polar Direct Drive (PDD) scheme proposed by the scientists from the LLE, Rochester [16] requires some significant modifications in the NIF focusing system that will affect the target design and its robustness. In that aspect shock ignition might have also some advantages compared to the standard direct drive PDD approach as the implosion velocity is lower and it thus imposes less stringent conditions on the implosion symmetry.

The paper is organized as follows: Section 2 is dedicated to the laser plasma interaction physics and numerical simulations of the laser absorption. Section 3 presents studies related to the hot electron transport, ablation pressure and the shock symmetry. The experiments on laser plasma interaction and the shock excitation are discussed in Sec. 4 of this review.

2. Laser plasma interaction

2.1. Theoretical estimates of interaction conditions

The particularity of shock ignition lies in the fact that a strong shock needs to be launched at the late time of shell implosion when the shell radius is reduced already by a factor of two. The shell is already compressed by a factor of ten or more. The characteristic profiles of the density, temperature, pressure and laser energy absorption rate are presented in figure 1(a). They are calculated for laser pulse profile shown in panel b at the moment of the laser spike arrival $t = 10.1\,\mathrm{ps}$. The target is shown schematically in figure 1(c). This is the baseline HiPER target designed in [3] for shock ignition.

The plasma corona has at that time a large extent of the order of $800\,\mu\mathrm{m}$, the characteristic density scale length in the absorption zone near the critical density is $L_n \sim 200\,\mu\mathrm{m}$, the distance between the absorption zone and the ablation surface is about $150\,\mu\mathrm{m}$, and the distance between the critical and quarter critical densities is about $300\,\mu\mathrm{m}$. The electron temperature of the corona is rather homogeneous and it exceeds the value of 2 keV. The ion temperature is $2-3$ times lower, at the keV level.

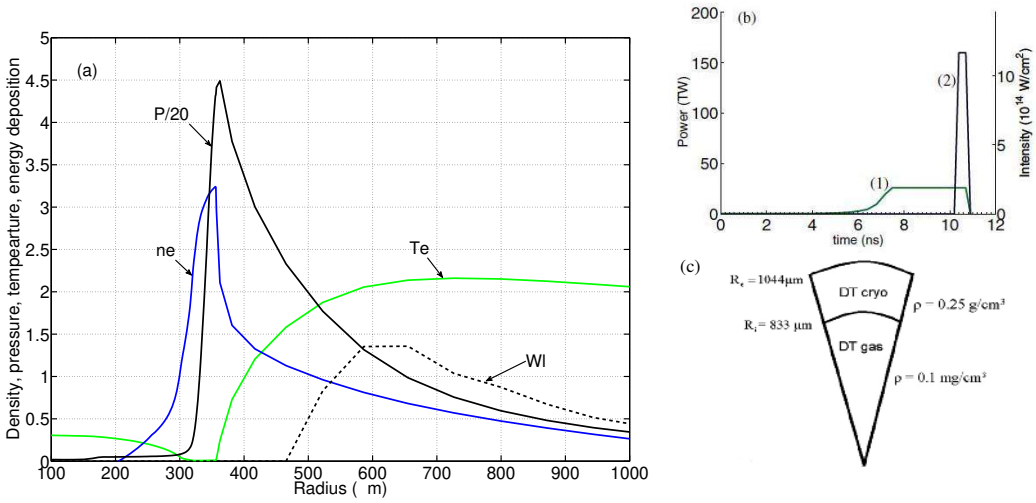

Figure 1. (Color online) a) Profiles of the plasma density, $\log(n_e/n_c)+1$ (in blue), the electron temperature T_e in keV (solid line, green), laser energy deposition W_L (dashed line) and the pressure p in Mbar divided by 20 (solid line, black) in function of the radius of imploding plasma at the time 10.1 ps of the spike arrival. The simulations are conducted with the radiation hydrodynamic code CHIC [17] for the laser wavelength of 0.35 μm. b) Temporal shape of the main laser pulse (1) and the laser spike (2). c) Scheme of the baseline all-DT HiPER target.

The standard linear mechanism of laser absorption in the plasma corona is due to the inverse Bremsstrahlung. it is described by the relation

$$dI/dz = -\kappa_{\rm IB} I \tag{2}$$

where $\kappa_{\rm IB} = (\nu_{ei}^c/c)\,(n_e/n_c)^2\,(1-n_e/n_c)^{-1/2}$ is the absorption coefficient, n_e is the electron density, ν_{ei}^c is the electron-ion collision frequency at the critical density $n_c = \epsilon_0 m_e \omega_0^2/e^2$, e and m_e are the elementary charge and the mass of electron, ϵ_0 is the permittivity of free space, ω_0 is the laser frequency, and z is the coordinate along the laser ray trajectory. The optical plasma thickness, $\tau_c = \nu_{ei}^c L_n/c$, defines the efficiency of collisional absorption. It is of the order of unity under the conditions of interest. That corresponds to the absorption $\eta_{\rm abs} \sim 70\%$ for the case of normal incidence. However for the PDD irradiation geometry, a large part of laser rays arrives at the oblique incidence and the total collisional absorption does not exceed $50-60\%$. Moreover, the nonlinear processes may significantly decrease this value.

The laser intensity required for launching the ignition shock wave exceeds the threshold of several parametric instabilities (such as SRS, TPD and SBS) that may reflect a significant portion of the laser light, filament laser beams creating high intensity spots, redistribute the laser energy over the absorption zone due to the cross-talk between the overlapping beams arriving from different directions. These processes may generate large amounts of energetic electrons due to the resonance absorption near the critical density and the parametric instabilities near or below the quarter critical density (SRS and TPD) [18]. The interaction parameter that is defining the efficiency of nonlinear processes is proportional to the quivering electron energy in the laser field, $\varepsilon_{\rm osc} = e^2 E_L^2/m_e\omega_0^2$, where E_L is the laser pulse amplitude. In the practical units, the quiver energy is proportional to the product $I\lambda^2$. The qualitative estimates

and experiments indicate that the parametric instabilities manifest themselves in enhanced light scattering and hot electron generation starting from the values of the interaction parameter above the level as low as $10\,\mathrm{TW}\mu\mathrm{m}^2/\mathrm{cm}^2$. However, they become the dominant effect in the laser energy absorption for the intensities one order of magnitude higher, that is, above $1\,\mathrm{PW}/\mathrm{cm}^2$ for the $3\,\omega$ laser radiation (the wavelength of $0.35\,\mu\mathrm{m}$). The inverse proportionality of the parametric instability thresholds with the laser wavelength explains an interest of using the short wavelength lasers for suppressing the nonlinear processes and enhancing the collisional absorption.

Self-focusing is an important process that can modify the propagation of a high power beam in a lower density part of plasma located in front of the absorption region. The technique of laser beam smoothing employed at high energy laser facilities by the random phase plates and smoothing by spectral dispersion [19], allows to suppress the global beam self-focusing by splitting the whole beam into multiple mutually incoherent beamlets with much smaller power. Self-focusing of the smoothed laser beam takes place in a focused beamlet (laser speckle) if the average speckle power $\langle P\rangle$ exceeds the critical power of the ponderomotive self-focusing

$$P_c = 34\,T_{\mathrm{keV}}(n_c/n_e)\sqrt{1-n_e/n_c}\,\mathrm{MW} \tag{3}$$

which is of the order of a hundred MW for the conditions of interest. For the typical focusing optics of the large scale installations $f/8$, the speckle radius is rather small about $2.5\,\mu\mathrm{m}$, nevertheless the average speckle power $\langle P\rangle \simeq 1\,\mathrm{GW}$ exceeds the critical power by a factor of 4 for the laser intensity $I_L = 5\,\mathrm{PW}/\mathrm{cm}^2$ in front of the absorption region. The effect of self-focusing on the laser beam energy deposition under such conditions implies that strong intensity enhancements may take place, but this was not yet studied in detail for the particular conditions of shock ignition.

The stimulated Brillouin scattering is the parametric instability corresponding to the decay of the incident electromagnetic wave into another electromagnetic and ion acoustic wave. Because of smallness of the ion acoustic frequency compared to the laser frequency, $\omega_s/\omega_0 \sim c_s/c \ll 1$, the SBS develops in whole plasma corona up to the critical density. Two processes – SBS in near forward and in backward or near backward directions are equally important. The forward SBS may develop even below the self-focusing threshold leading to strong beam spraying [20, 21]. Similarly to self-focusing, this is a non-stationary process resulting in reduced local laser intensity inside the plasma and reduced collisional absorption. These considerations indicate that some strategy must be identified to control self-focusing and beam spraying, like using a shock laser pulse with a smaller f-number or a smaller wavelength. The use of a broadband laser smoothing through spectral dispersion and multiple polarizations has been shown to be efficient and should be taken in consideration [22].

The stimulated Brillouin scattering in backward direction is one of principal laser energy losses in the plasma corona. Its performance depends strongly on the velocity and temperature profiles in expanding plasmas and on the spatial and temporal structure of the laser beam. It develops in high intensity laser speckles and manifests itself in periodic bursts of reflectivity.

The stimulated Raman scattering corresponds to the decay of the incident electromagnetic wave into another electromagnetic wave and an electron plasma wave. The frequency of the SRS light, ω_{SRS}, is red shifted with respect to the laser light by the local plasma frequency, ω_{pe}, that is, $\omega_{\mathrm{SRS}} = \omega_0 - \omega_{pe}$. That provides a relation between the SRS wavelength and the plasma density

$$\lambda_{\mathrm{SRS}} \simeq \lambda_0\,[1-(n_e/n_c)^{1/2}]^{-1}. \tag{4}$$

Thus the spectral shift of the SRS light provides an information about the plasma density.

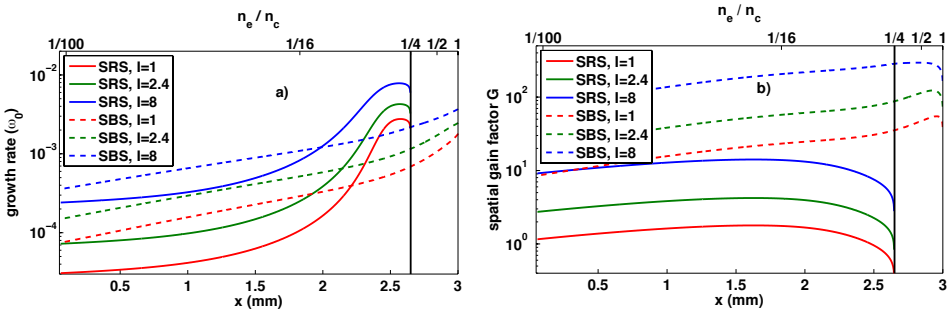

Figure 2. (Color online) Growth rates (a) and gains (b) for SBS and SRS backscattering versus the spatial coordinate along the density profile (the corresponding density is shown in the upper axis). The intensity in the legend is in the units of PW/cm^2. The parameters of plasma correspond to the profiles shown in figure 1(a). The gain Eq. (5) is limited by the wavenumber mismatch, which is due to inhomogeneity in the hydrodynamic velocity (in the case of SBS) or in the plasma density (in the case of SRS).

The SBS and SRS instabilities are characterized by their growth rates and spatial gains. In an inhomogeneous plasma the resonance conditions are fulfilled in a narrow zone depending on the gradient length and the scattered wave frequency. The growth rates of SBS and SRS are highest for backscattering. This justifies a one-dimensional approach, which is often used to study these instabilities. The instability growth rates are compared with the rates of damping of the daughter waves, which include both collisional and Landau damping, in figure 2(a). The SRS growth rates are relatively high in the plasma in front of the quarter critical density. They attain their maximum in a 1 mm wide region, which corresponds to plasma density $\sim 0.2\, n_c$. In the lower density plasma, the growth of backward SRS is strongly reduced by the Landau damping of the electron plasma wave. This is a particular feature of a high temperature plasma where the kinetic parameter, $k_p\lambda_D$ is relatively high. Here, k_p is the plasma wave number and λ_D is the Debye wavelength.

Although SRS is strongly suppressed in high temperature Maxwellian plasma, it may reappear in non-equilibrium conditions where the electron distribution function is modified by the plasma waves creating a plateau in the velocity domain corresponding to the resonance interaction with SRS-excited plasma waves. Then the growing SRS further suppresses the Landau damping leading to the explosive evolution of the scattering process. This effect called "inflationary SRS" [23] has been discussed in application to the indirect drive experiments. However, it is also important in the shock ignition conditions where a high intensity laser spike interacts with a hot plasma corona.

The growth rates for SBS are not so high as for SRS. It is partially related to the fact that ion acoustic waves in the underdense plasma are suffering the collisionless Landau damping. Nevertheless, at the transitional stage of interaction strong SBS spikes may be generated near the critical density. They are propagating all over the plasma and carrying out large amounts of the laser energy.

The spatial amplification of daughter waves induced by stimulated scattering in

an inhomogeneous plasma is described by the Rosenbluth gain factor

$$G = \frac{\pi\gamma_0^2}{|\Delta k' v_{g1} v_{g2}|} \tag{5}$$

where γ_0 is the temporal growth rate in a homogeneous plasma, $\Delta k'$ is the spatial derivative of the wave numbers of three interacting waves in the resonance point $\Delta k = 0$, and $v_{g1,2}$ are the group velocities of the scattered and daughter plasma waves. Whereas the inhomogeneity in plasma density governs the convective amplification of SRS wave, the spatial amplification of SBS wave is usually limited by the inhomogeneity in the hydrodynamic velocity. The SBS gain plotted in figure 2(b) is rather high but it takes place at high plasma densities that may be screened by the SRS. The convective amplification of SRS might be quite significant at intensities above $5\,\mathrm{PW/cm^2}$ if Landau damping does not suppress the growth of electron plasma waves.

Special attention is required in the zone of quarter critical density where, in addition to SRS, the two plasmon decay (TPD) can be excited. The threshold for TPD in an inhomogeneous profile is given [24, 25]

$$I_{\mathrm{thTPD}} = 5\,T_{\mathrm{keV}} L_n^{-1} \lambda_{\mu\mathrm{m}}^{-1}\,\mathrm{PW/cm^2} \tag{6}$$

where the electron temperature in the quarter critical density is in keV, and L_n and $\lambda_{\mu\mathrm{m}}$ are in microns. Moreover, SRS in the quarter critical density becomes also an absolute instability with a quite low threshold [26]

$$I_{\mathrm{thSRS}} = 120\,L_n^{-4/3} \lambda_{\mu\mathrm{m}}^{-2/3}\,\mathrm{PW/cm^2}. \tag{7}$$

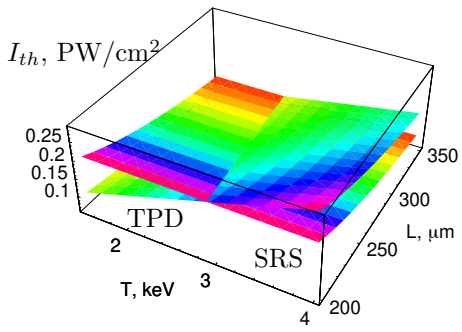

Figure 3. (Color online) Thresholds of the SRS and TPD instabilities in function of the plasma scale length and the temperature for the shock ignition conditions at the wavelength of $0.35\,\mu$m.

Figure 3 demonstrates the dependence of the thresholds of both instabilities on the plasma temperature and the density scale length. Both thresholds in the shock ignition domain are comparable and they are $5-10$ times below the typical intensity of $1\ \mathrm{PW/cm^2}$. Moreover, the TPD dominates for the temperatures below $2-3$ keV, while the SRS is more important for higher temperatures. For these conditions the parametric instability in the quarter critical density evolves in a hybrid mode that combines both SRS and TPD as the limiting cases [27, 28]. In the transient domain the direction of maximal growth depends on the plasma temperature and the scale

length. However, the maximum growth rate well above the threshold is the same for both instabilities, $\gamma_{\max} \simeq 11\, I_{PW}^{1/2}$ ps [29].

Numerical studies of the competition between SRS and TPD require multidimensional simulations [29, 30]. They demonstrate that the TPD is effective on the transient stage of a few ps. This was evidenced by the spectral distribution of the plasma waves and the energy and the number of hot electrons. Later in time the SRS dominated the plasma response. Similar conclusion has been reported in the experimental paper [31], where a correlation between the hot electron production and the generation of the $3\omega/2$ harmonic (the signature of TPD) was reported in the very beginning of the laser pulse when the plasma was sufficiently cold, while a correlation of hot electron production with the SRS emission was seen later in time.

In the following section we present the results of a series of numerical simulations with PIC codes in one and two spatial dimensions dedicated to the studies of the effect of parametric instabilities under the shock ignition conditions.

2.2. Numerical simulations of laser plasma interaction: SRS and SBS competition

Fully kinetic collisional simulations are performed using a massively parallel relativistic electromagnetic PIC code in one-dimensional geometry [32, 33]. The simulations are sufficiently long (several tens of picoseconds) so that a quasi-steady state may be established in the interaction. Specially designed absorbing boundary conditions at the rear side of the simulation box allow us to evaluate the number of hot electrons and the energy transported to denser plasma. This boundary condition is used to absorb the increased flux of kinetic energy due to laser absorption and provide the return current with a constant temperature equal to the initial one. Numerical heating is suppressed by using the higher order shape forms for the particles.

The plasma conditions are taken similarly as in [33] from the hydrodynamic simulations of recent shock ignition experiments on Omega laser facility [34]. The profile of electron density is approximately exponential in the underdense part of plasma with the scale length of about $150\,\mu$m. The electron temperature ranges between 1.6 and 2.1 keV with the maximum at about $0.3\,n_c$. The ion temperature and hydrodynamic velocity profiles have almost linear shapes (the temperature decreasing and the velocity increasing with the distance from the target). The ion temperature ranges between 0.4 and 1.2 keV and the expansion velocity between 150 and 1050 km/s.

In simulations, the laser pulse intensity was 1, 2.4 or 8 PW/cm^2 at the wavelength of 350 nm. The laser pulse had a 5 ps long linear ramp at the beginning and than it stayed on the maximum intensity. The ion charge and the ion mass were assigned values of $Z = 3.5$ and $m_i = 7\,m_p$, respectively, where m_p is the proton mass. That corresponds to the average ion in a fully ionized CD shell. The simulations were performed with relativistic Coulomb intra- and inter-species collisions, which have been tested in simulations of laser absorption in a homogeneous plasma [32].

2.2.1. Lower intensity domain – 1 PW/cm^2

The collisional effects are important in the low intensity domain. The simulations were performed also with the collisional algorithm turned off to demonstrate the effect of collisions in this case. The temporal behavior of overall reflectivity in the collisional and collisionless simulations is presented in figure 4(a). The theoretical value obtained as $1 - \eta_{\text{abs}}$, where η_{abs} is the inverse Bremsstrahlung absorption coefficient calculated according to (2), is included for comparison. The average reflectivity is more than 60%

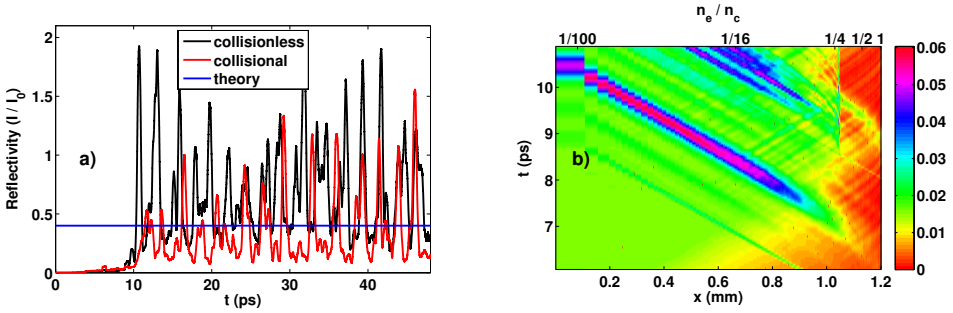

Figure 4. (Color online) a) Temporal evolution of reflectivity in the collisional and collisionless simulations of laser plasma interaction at the intensity 1 PW/cm^2. The reflectivity calculated from the inverse Bremsstrahlung theory is included for comparison. b) Temporal evolution of the electromagnetic field energy density (in arbitrary units) inside the target in the collisionless simulation with 1 PW/cm^2.

in the collisionless case and the reflected light comes in a series of intense pulses, which originate from the convectively amplified SBS waves. The amplitude of reflectivity is much smaller and the average value is little less than 30% in the collisional case comparable with the reflectivity expected from the inverse Bremsstrahlung theory.

The origin and amplification of SBS in the collisionless simulation are clearly seen in the temporal evolution of electromagnetic field energy density inside the target as shown in figure 4(b). This figure demonstrates the first strong pulse, which is observed in the reflectivity at about 11 ps. This SBS pulse starts at about 1.1 mm corresponding to the density of about $0.4-0.6\ n_c$ and it is strongly amplified during the first 0.3 mm of propagation to the density of about $0.1\ n_c$. The pulsating behavior of SBS has been reported in [35] and it is explained by a strong convective gain of the scattered wave which depletes completely the pump on its way out of plasma. The strength of the light pulses scattered by SBS is much weaker in the collisional case as the collisional damping of both, the incident and also the scattered light wave in the denser plasma is comparable to the SBS growth rate.

An efficient heating of the bulk population of electrons due to collisional absorption of the incident laser pulse is confirmed by analysis of the energy distributions of electrons, $dn_e/d\varepsilon$, in the simulation box. Figure 5(a) presents the averaged over the angles the electron distribution function

$$\frac{dn_e}{d\varepsilon} = \int d\vec{\Omega}\, \frac{v^2}{p}\, f_e(\vec{v}) \tag{8}$$

in the initial time and the time of 50 ps. Here $\vec{\Omega} = \vec{v}/v$ is the unitary vector in the velocity direction, $p = m_e v$ is the electron momentum, and $f_e(\vec{v})$ is the electron distribution function. The electron energy distribution has an exponential profile corresponding to a Maxwellian function. The initial temperature is 2 keV, while the temperature at 50 ps is increased to about 2.4 keV. Thus, the laser plasma interaction at 1 PW/cm^2 is dominated by collisions. The laser pulse is efficiently absorbed due to inverse Bremsstrahlung in the higher density plasma (above $1/4\ n_c$). The collisions suppress the SRS instability, and the resulting reflectivity (which is less than 30%) is largely dominated by SBS.

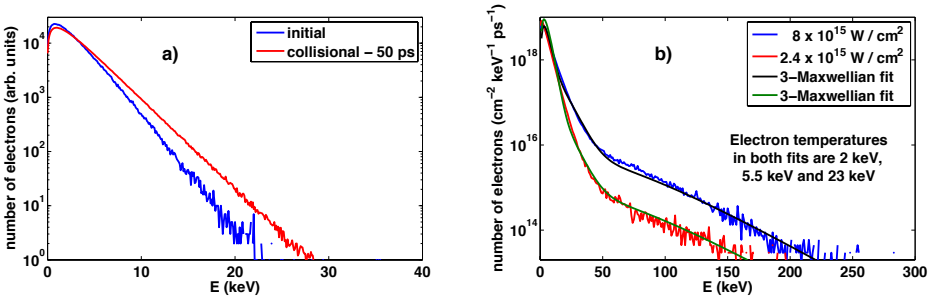

Figure 5. (Color online) a) Electron energy distributions in the simulation box, $\ln(dn_e/d\varepsilon)$, at the beginning and at the end of the collisional simulation with the laser pulse intensity 1 PW/cm^2. b) Temporally averaged differential flux of electrons flying into the target for the laser pulse intensity 2.4 (red) and 8 PW/cm^2 (blue) recorded close to the rear side of the target in simulations with higher intensity. The distributions are interpolated as a sum of three Maxwellian distributions with the temperatures 2, 5.5, and 23 keV. Note the different energy scales in panels a and b.

2.2.2. Higher intensity domain – 2.4 and 8 PW/cm^2

Importance of parametric processes increases with increasing laser pulse intensity, while the collisional processes become less important. This transition manifests itself by the appearance of hot electron tail in the energy distribution function and it is observed while changing the laser pulse intensity from 1 to 8 PW/cm^2 through the intermediate case at 2.4 PW/cm^2 and keeping the same initial temperature and density profiles [33]. The time averaged differential (in energy) electron flux,

$$\Psi(\varepsilon) = \int d\vec{\Omega}\, \frac{v^2}{p}\, v_x f_e(\vec{v}) \tag{9}$$

where the integral is taken over the hemisphere $v_x > 0$, is shown in figure 5(b). It is recorded in the simulations close to the target rear side. This flux can be interpolated with three Maxwellian-like components. The bulk thermal electrons keep the initial temperature of 2 keV, there is an intermediate population with the temperature of 5.5 keV and the hot electrons having the temperature of 23 keV.

It is important to note that the effective temperature of hot electrons practically does not depend on laser intensity in the range of intensities considered here, while the hot electron number increases linearly with the absorbed laser pulse energy. There are virtually no hot electrons at the lowest laser intensity as it is shown in figure 5(a), while at higher intensities an increasing fraction of the absorbed energy is transported into the target with the electrons having approximately the same effective temperature.

The distribution function of the electrons carrying energy in the dense plasma can be characterized by the differential energy flux that is described by the function

$$\frac{dq_x}{d\varepsilon} = \varepsilon \int d\vec{\Omega}\, \frac{v^2}{p}\, v_x f_e(\vec{v}) \tag{10}$$

where $\varepsilon = m_e v^2/2$ is the electron kinetic energy and the integral is taken over the all angles. It is shown in figure 6 for the laser intensities of 2.4 and 8 PW/cm^2. This function was time averaged over the last 15 ps of the simulation time. The energy in the dense plasma is carried out with the electrons having energies above $\sim$ 15 keV. The energy of electrons carrying the maximum energy increases from 21 to 25 keV in the

considered range of laser intensities. Taking into account only electrons with energies above 30 keV, the part of energy transported by hot electrons found in our simulations is about 25% and 70% of the laser pulse energy for the intensities 2.4 and 8 PW/cm^2, respectively. However, a significant part of this energy flux is compensated with the return current of colder electrons. For example, the total electron energy flux through the right boundary in the latter case is 2.3 PW/cm^2, or only 28% of the incident laser energy.

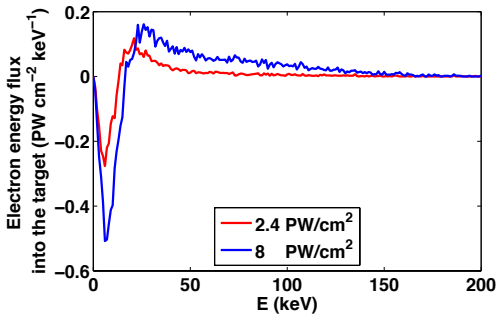

Figure 6. (Color online) Temporally averaged differential energy flux of electrons in the collisional simulations of laser plasma interaction with the laser pulse intensity 2.4 (red) and 8 PW/cm^2 (blue).

It could be that 1D simulations overestimate the role of the parametric absorption and hot electron generation. As it is shown in the next section, the cavitation process is weaker in 2D, and the effects like self-focusing and filamentation modify the interaction dynamics.

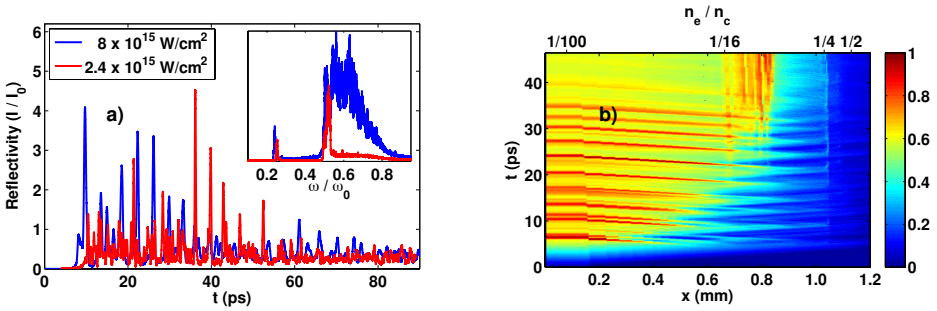

Figure 7. (Color online) a) Temporal evolution of the reflectivity in the collisional simulations of laser plasma interaction with the laser pulse intensity 2.4 and 8 PW/cm^2. The inset contains the temporally integrated spectra of the reflected light in the SRS domain. b) Temporal evolution of the electromagnetic field energy density inside the target in the simulation with the intensity 8 PW/cm^2. The energy density is in arbitrary units.

Laser plasma interaction in the higher intensity domain proceeds through two successful steps, which are demonstrated in the temporal evolution of reflectivity in figure 7(a). The first one is a transient stage with a high reflectivity (80%) dominated by the SBS. It is followed by a quasi-steady stage with a higher absorption (70%) dominated by the SRS and cavitation. For our initial conditions, SBS has much higher

gain than SRS and its growth is not suppressed significantly during the initial transient stage. Therefore, this instability backscatters most of the pump wave energy and the reflectivity is rather high. The SRS is an absolute instability at $1/4\,n_c$ and it is growing in the meantime. When the local field induced by this instability becomes high, it expels electrons and the subsequent Coulomb explosion of ions produces density cavities, which partially trap the light and accelerate the particles [32]. The cavities are first produced at $1/4\,n_c$.

The inset in figure 7(a) contains the power spectra of reflected light in the SRS domain. One can distinguish here three different signals. In the spectral range $0.6 - 0.8\ \omega_0$, the signal is due to convective SRS from lower density plasma (below $1/4\,n_c$). It is observed that the signal in this domain strongly depends on laser intensity. As already noted, this convective SRS is strongly suppressed by Landau damping. Therefore, it is not observed at lower intensities, while at higher intensity the electron distribution function is strongly modified and SRS can take place in the inflationary regime [23]. Two other signals at $0.5\ \omega_0$ and $0.25\ \omega_0$ are due to absolute SRS at $1/4\ n_c$ and its Raman cascade, which is explained below.

The light scattered from the quarter critical density (with frequency $0.5\,\omega_0$) propagates back along the density profile, and if its intensity is not very high it leaves the plasma. However, when the intensity of this light overcomes the SRS threshold, it may be scattered again on its way back at $1/16\ n_c$, which is its own $1/4\ n_c$. The scattered light can only propagate down the density profile and if its intensity is still sufficient, the process may proceed the same way by the next stage in the Raman cascade at $1/64\,n_c$. The absolute SRS taking place at $1/16\ n_c$ results also in cavitation, which is even stronger than at $1/4\ n_c$ at later times $t > 30$ ps for 8 PW/cm^2.

During the second quasi-steady part of interaction, the reflectivity is reduced due to the cavitation in lower density plasma as the cavities discontinue the spatial amplification of SBS waves. This can be seen in figure 7(b) where the temporal evolution of electromagnetic field energy density is plotted. The flashes due to SBS (propagating out of the target to the left) are clearly observed during the transient stage, which lasts for about 35 ps. The cavities around $1/16\ n_c$ start to develop at about 30 ps. They can be clearly observed in the figure as vertical strips as they trap a significant electromagnetic energy.

The absorption of the laser pulse becomes quite efficient (70%) in the quasi-steady stage of interaction after the cavities develop. Most of the absorbed energy goes into hot electrons with a temperature in the $20 - 30$ keV range as shown in figure 5(b). The absorption takes place in particular in a low density plasma, and it is due to the convective SRS that is developing in the inflation regime and the absolute SRS around the 1/4 and the 1/16 of n_c, that is trapping strong electromagnetic fields in cavities.

2.3. Two-dimensional simulations of laser plasma interaction

Plasma cavitation under the ponderomotive pressure of SRS-excited plasma waves is identified as the prime mechanism of strong suppression of SBS and efficient laser energy absorption in 1D simulations with higher laser intensity. However, the 1D geometry excludes the possibility of the TPD, SRS side scattering, filamentation and self-focusing and also cavity expansion in transverse directions. The 2D PIC simulations of the laser plasma interaction were performed to understand the importance and the interplay of these processes [29, 36]. The results of 1D simulations indicate that the most important processes in laser plasma interaction at higher

intensities take place in a lower density plasma $n_e \lesssim 1/4\ n_c$. This enables to restrict the volume of plasma in the 2D case, which in turn enables to treat time scales of several ps.

The 2D full PIC simulations performed with the code EMI2D [37], use the laser and plasma parameters similar to that discussed in the previous section. The simulated plasma region extends 160 μm in the laser propagation direction and 103 μm in the transverse direction. The exponential plasma profile has a scale length of $L_n \approx 60$ μm, extending from 0.04 n_c up to 0.4 n_c, with 60 particles per cell for the highest density value. Electron and ion temperatures are 5 keV and 1 keV, respectively. The case that is discussed here corresponds to the laser intensity of 40 PW/cm^2, which are higher than in the 1D case, as the simulations are modeling a single laser speckle with a full width at half maximum (FWHM) of 29 μm.

The 2D simulations [36], similarly to the 1D case, show a fast development of the SRS and SBS instabilities manifesting themselves in strong reflectivity bursts, see figure 8(b), during initial few ps of interaction. The SBS dominates the reflectivity starting from the first picosecond as it is less sensitive to the density inhomogeneity and high temperatures. However, as time goes on, the SBS bursts become less violent as the amplification is inhibited by the cavitation process developing in 1/4 n_c.

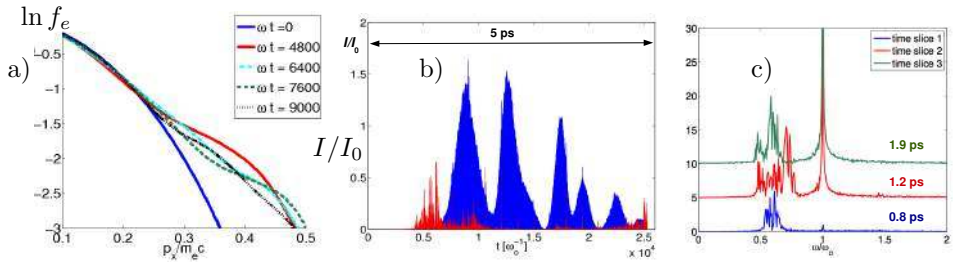

Figure 8. (Color online) 2D simulation of interaction of the laser speckle with the intensity 40 PW/cm^2 with an inhomogeneous plasma: a) Electron distribution function in the simulation box at the time moments of 0 (blue), 0.80 (red), 1.05 (dashed light blue), 1.3 (dashed green) and 1.5 ps (dashed black). The blue line correspond to the Maxwellian distribution with the temperature of 5 keV. b) Temporal evolution of the reflectivity. The SBS component ($> 0.9\,\omega_0$) is shown in blue, the SRS part ($< 0.9\,\omega_0$ – in red. c) Three snapshots of the electromagnetic field spectrum emitted from the center of speckle.

Before the SBS has time to grow up, the spectrum in figure 8(c) shows that the SRS from the $1/4\,n_c$ dominates the response. However, later in time the SRS spectrum broadens significantly indicating SRS contribution from a low density plasma $n_e \sim 0.22 - 0.05\ n_c$. This is manifestation of inflationary SRS, which corresponds to scattering from short wavelength plasma waves that were initially strongly damped because of their low phase velocity ($k\lambda_D \lesssim 0.7$). The fast electrons generated in the near $1/4\,n_c$ region decrease the damping of a broad spectrum of plasma waves as they spread over the plasma and facilitate the SRS excitation. The light scattered by the inflationary SRS has a wide angular distribution with opening angles up to 45°.

Destabilization of the SRS in a low density plasma can be seen in the electron distribution function in figure 8(a). Flattering of the electron distribution in the velocity range of $0.2 - 0.3\,c$ (the electron energies $10 - 25\,$keV), corresponds to the reduction of Landau damping for the plasma waves with phase velocities $2 - 3$ times

the electron thermal velocity. These are the waves that are responsible for the late time SRS. A similar scenario of SRS destabilization by hot electrons has been discussed in large scale multi-speckle simulations [38, 39]. In their case of a large, homogeneous, low density ($n_e/n_c \sim 0.12 - 0.14$) plasma the electrons produced in the SRS process in a high intensity speckle destabilized smaller neighbor speckles with intensities even below 1 PW/cm^2. It is quite possible that the SRS will also develop at lower intensities in the shock ignition conditions if one considers a multi-speckle laser beam.

The specificity of 2D simulations is in the simultaneous excitation of the absolute SRS and TPD. As their growth rates under the shock ignition conditions are comparable, according to Sec. 2.1, both instabilities are excited as soon as the laser radiation attains the quarter critical zone [29]. They can be clearly distinguished in the wave spectrum as the TPD plasma waves have larger wave vector components perpendicular the density gradient that depend on the frequency detuning between the half of laser frequency and the local plasma frequency.

However, both the absolute SRS and TPD are quickly saturated due to the cavitation process. In 2D simulations, compared to 1D case, the interference of electron plasma waves induced by the TPD facilitates the cavitation. Because of symmetry of plasma wave excitation in the plane perpendicular to the density gradient, the oppositely traveling pairs of plasma waves interfere thus creating quasi-neutral modulations with the scale equal to a half of their perpendicular wavelength, see figure 9. These electron density modulations are seeding the cavities. Thus cavitation spans over a large region of plasma below $1/4$ n_c producing small-scale density depressions filled with high intensity electromagnetic waves. Unlike in 1D simulations, the cavitation in 2D is unstable. After trapping the light, the cavities transfer their energy to electrons and ions, expand and disappear on the characteristic time scale of a few ps. The cavitation-induced density perturbations in the vicinity of $1/4$ n_c have the function of a dynamic random phase element, which affects spatial and temporal coherence of the electromagnetic waves in plasma. In particular, it inhibits the SBS amplification and reduced strongly the plasma reflectivity.

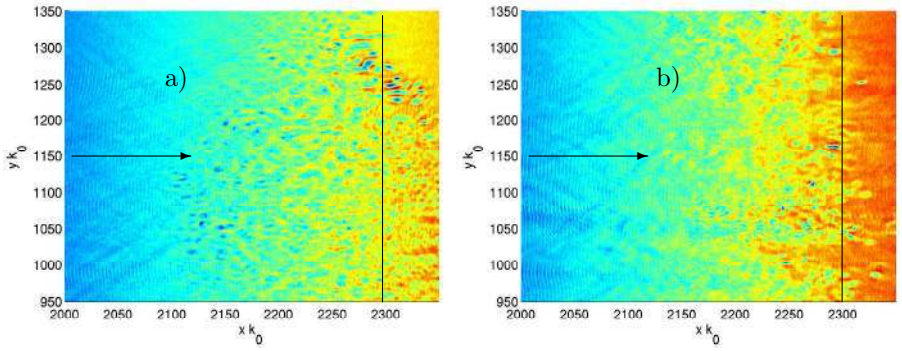

Figure 9. (Color online) Density modulations in the zone $1/4\,n_c$ at the time moments of 0.9 (left) and 2.4 ps (right). The cavity's size is much smaller than the speckle size and they are elongated parallel to the density gradient (horizontal axis) due to the TPD seeding. The laser comes from the left. The picture size is $20 \times 22\,\mu$m^2. The vertical line shows the initial position of the quarter critical density. The speckle axis is indicated by the arrow. The maximum depth of cavities is about 50% of the average density.

In the initial stage of the laser plasma interaction, laser absorption takes place around $1/4\ n_c$ due to absolute SRS, TPD and cavitation. Later in time the inflationary SRS at the densities around $0.1\ n_c$ contributes to the formation of hot tail in the electron energy distribution. As it is shown in figure 8(a), the hot electron temperature is about $30 - 50$ keV and the electron energy distribution is cut at the energies less that $150 - 200$ keV, which is in agreement with 1D simulations. Thus the presence of SRS, TPD and cavitation do not seem to be detrimental to the shock-ignition scenario as far as the preheating of the compressed fuel is concerned. However, the laser plasma interaction in 2D simulations is dominated by SBS on the longer time scales of several ps resulting in a rather high reflectivity exceeding 50%. Although the SBS activity seems to be decreasing with time, a long-term behavior of reflectivity and SBS saturation in relation to the dynamic cavitation need further studies.

The cavitation mechanism of parametric instability saturation seems to be quite robust and takes over other processes as soon as the laser intensity is sufficiently high, above a few times the level of PW/cm^2. In contrast, very close to the TPD threshold, the level of plasma wave turbulence is relatively low and the cavitation was not observed [30].

In summary, starting from the laser intensities of several PW/cm^2, the laser plasma interaction is dominated by collective effects. After the initial transient period of several picoseconds, the plasma cavitation develops due to absolute SRS and TPD at $1/4\ n_c$ and interaction enters into the quasi-steady phase. The laser pulse is efficiently absorbed due to inflationary SRS and cavitation. Both these processes accelerate electrons to suprathermal velocities thus producing hot electrons with approximately Maxwellian energy distribution with the temperature in the range $20 - 30$ keV and the cut-off near $150 - 200$ keV. Increasing the laser pulse intensity, the absorption and the hot electron temperature remain the same, while the number of hot electrons correspondingly increases.

3. Ablation physics

3.1. Hot electron transport and preheat

The laser energy absorbed in the plasma corona is transported to the dense target with electrons. We distinguish three types of electrons in the energy transport: (i) the thermal electrons with the mean free path smaller than the distance between the energy deposition zone and the dense shell; (ii) the fast electrons that penetrate the shell, but have the mean free path smaller than the shell thickness, and (iii) very energetic electrons that cross the shell and depose their energy homogeneously. Figure 1 obtained in the simulations of shock ignition with the laser wavelength of $0.35\,\mu$m shows that the shocked region where the pressure is maximal, ~ 100 Mbar, is located at the distance of about $200\,\mu$m from the energy deposition zone. The maximal density rises by a factor ~ 400 compared to the critical density. The shell density is exceeding 10 g/cm^3 and its thickness is $\sim 30\,\mu$m.

The electron thermal transport in ICF hydrodynamic simulation codes is described commonly with the flux-limited model [40]. The electron energy flux in such a model is calculated as a minimum between the Spitzer-Härm heat flux, $\mathbf{q}_{\rm SH} = -\kappa_{\rm SH}\nabla T_e$, proportional to the electron temperature gradient, and a fraction $f < 1$ of the free-streaming limit: $\mathbf{q}_f = -n_e T_e v_{the}\nabla T_e/|\nabla T_e|$, where $v_{the} = (T_e/m_e)^{1/2}$ is the electron thermal velocity. The typical value used to simulate the direct-drive

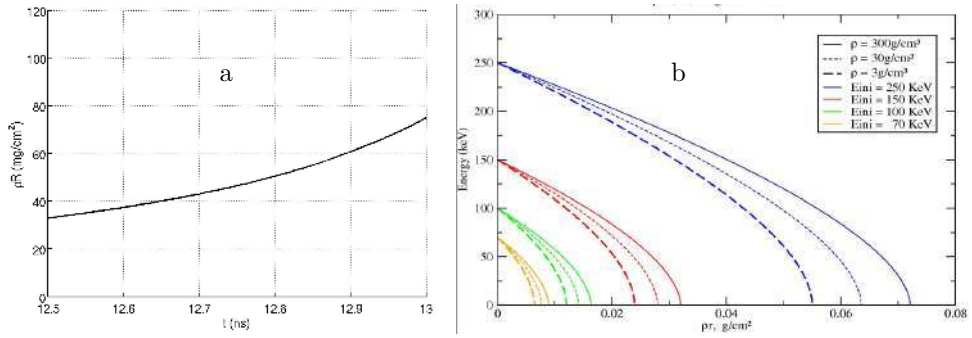

Figure 10. (Color online) a) Time evolution of the shell areal density during the implosion of a DT target of the NIF-LMJ scale. b) Stopping power of electrons with the energies of 70, 100, 150 and 250 keV in a DT plasma with the density 3, 30 and 300 g/cm^3.

implosion is $f = 0.06$. Although the value of flux limiting factor does not affect directly the ablation pressure, it affects the corona temperature and thus the efficiency laser absorption and the role of parametric processes.

The ablation pressure driven by the thermal electrons can be estimated from Eq. (1) derived in Ref. [8]. In this model, the laser energy flux is deposited near the critical density $\rho_c = m_i n_c$. Here, the expansion plasma velocity is equal to the local sound velocity c_s, and the absorbed laser energy flux $I_{\rm abs}$ is related to the energy flux carried with the plasma flow as: $I_{\rm abs} \simeq 4\rho_c c_s^3$, where $c_s = (T_e/m_i)^{1/2}$ is the ion acoustic speed. Thus the corona temperature scales as: $T_e \propto (I_{\rm abs}/\rho_c)^{2/3}$. This expression, however, does not account for fast electrons that have the mean free path comparable with the size of heat conduction zone and need to be considered separately.

The shock pressure of more than $300 - 400$ Mbar is needed to achieve ignition. Assuming the laser wavelength $\lambda = 0.35\,\mu$m and the absorption $\eta_{\rm abs} = 60\%$, the scaling law (1) indicates that laser intensities higher than $7-10\,$PW/cm^2 are necessary. These values are evidently well above the threshold of parametric instabilities, and hot electron generation in corona may modify the spike pressure significantly.

The role of hot electrons in the shell implosion has been studied in 1980s in the experiments with the CO_2 laser [42, 43]. Because of a long wavelength of 10.6 μm, the laser interaction parameter $I\lambda^2$ was very large and the nonlinear effects dominated the interaction already at the intensities below 0.1 PW/cm^2. Copious hot electrons were crossing the target and preventing the shell from an efficient implosion. This effect was the main reason of abandoning the CO_2 lasers in the ICF research. However, it was already noticed at that time that hot electrons could generate a high ablation pressure if stopped in the shell [44, 45, 46, 47].

Situation with hot electrons in the context of shock ignition is different from that has been seen with the CO_2 lasers. Figure 10(a) shows the areal density of the shell during the laser spike interaction with the DT target of the LMJ-NIF scale. It varies in the range from 30 to 80 mg/cm^2. As it can be seen in figure 10(b), the areal density of 30 mg/cm^2 corresponds to the range of electrons with energies ~ 150 keV. Thus the electrons with energies below 100 keV will be stopped in the shell and will not preheat it. Instead they may contribute to the ablation pressure [3, 48].

As it was discussed in Secs. 2.2 and 2.3, there are two hot electron sources in the corona related to the SRS and TPD instabilities. The hot electrons generated by the SRS are expected to have a quasi-Maxwellian distribution with the characteristic temperature $\sim 30 - 50\,\mathrm{keV}$. In contrast, the TPD electrons are more energetic and may contribute to the target preheat. However, according to studies of SRS-TPD competition presented in Sec. 2.3, the TPD instability is excited at the transient stage of evolution and then it is suppressed by the caviton formation.

Thus, hot electrons in the shock ignition scenario may provide a useful contribution to the shock pressure. However, this issue is not yet studied in detail. The pressure formation by hot electrons in a dense plasma was described by the Fokker-Planck kinetic equation coupled to cold fluid ions in Ref. [49]. It was found that non-local effects are significant in the heat front regime and might lead to formation of high pressures of a several hundred Mbar. However the heat front regime corresponds to very short times before the shock formation. One has to consider longer electron beams for evaluation of their efficiency for the shock drive.

The particularity of hot electron energy deposition is that their stopping distance λ_e depends only on the hot electron energy ε_e and the electron density n_e:

$$\lambda_e \simeq 4\pi\psi\epsilon_0^2\varepsilon_e^2/e^4 n_e \ln\Lambda \tag{11}$$

where ψ is a numerical factor of the order of 1 in a DT plasma and $\ln\Lambda$ is the Coulomb logarithm. Consequently, the areal mass of the target heated by fast electrons depends only on their energy. Assuming that the shell areal density is larger than $\rho_s\lambda_e$, the electrons will heat a small part of the shell launching the shock inside and the rarefaction wave outside. The dynamics of the shock launched by a beam of energetic electrons in a dense solid shell was considered recently in Ref. [50].

The characteristic time needed to create a pressure and to launch a shock is defined by the time the rarefaction wave crosses the heated region, $t_h \simeq \lambda_e/c_s$. For a given electron beam energy flux I_b, this time reads: $t_h \simeq \lambda_e\rho_s^{1/3}I_b^{-1/3}$. At that time the maximum pressure is created in the shell. Later in time the shock pressure decreases as $t^{-1/2}$ as the remaining part of the electron beam energy is absorbed in the expanding plasma. Therefore, t_h is the optimal time of shock excitation by the beam of hot electrons. The pressure at that moment can be evaluated as

$$p_h \simeq I_b t_h/\lambda_e \simeq 0.4\,\rho_s^{1/3}I_b^{2/3}. \tag{12}$$

Although this pressure scales with the intensity in the same way as the one created with thermal electrons in Eq. (1), this pressure is much higher as the fast electrons depose their energy in a much denser plasma. For example, in a shell with the density $\rho_s = 10\ \mathrm{g/cm^3}$ the electron beam with the intensity of $1\ \mathrm{PW/cm^2}$ creates a pressure of the order of 400 Mbar. For electrons with the characteristic energy of 70 keV, the stopping power in DT shell is $\rho_s\lambda_e \simeq 8\,\mathrm{mg/cm^2}$, cf. figure 10. Then, the thickness of hot electron ablated layer is $8\,\mu\mathrm{m}$ and the heating time $t_h \simeq 80\,\mathrm{ps}$. The efficiency of shock excitation by fast electrons is of the order of 10%.

Another positive effect of hot electrons with energies below 100 keV is the ablation pressure symmetrization. During the power spike, the distance between the critical surface and the ablation front is larger than $200\,\mu\mathrm{m}$. This distance is comparable with the shell radius [3]. Then the hot electrons generated in corona in high intensity laser spots will spread over the shell surface and smooth out the intensity perturbations.

Very energetic electrons with the ranges comparable or larger than the shell areal density at the time of spike launch are harmful as they provide a homogeneous shell

heating thus degrading the implosion. According to figure 10, these are the electrons with the energies above $150-200$ keV that are created near the quarter critical density due to the TPD instability. The preheat effect can be illustrated as follows. The shell heating by fast electrons can be considered as an isobaric process, $p_s \simeq$ const. The shell pressure, $p_s \propto \alpha\rho_s^{5/3}$, is proportional to the adiabat parameter α and the shell density ρ_s. The shell internal energy $\mathcal{E}_s \propto \alpha M_s \rho_s^{2/3}$, is proportional to the shell mass, M_s, and the ratio of p_s to ρ_s. Thus, the shell density variation, $\Delta\rho_s$, is proportional to the hot electron energy deposited in the shell, $\mathcal{E}_{\rm hot}$:

$$\Delta\rho_s/\rho_s = -5\Delta\alpha/3\alpha = -\mathcal{E}_{\rm hot}/\mathcal{E}_s.$$

The areal density of compressed shell ρR is proportional to the square of the compression factor $C = R_s/R_{\rm min}$, which itself is proportional to the square root of the ratio of the shell kinetic energy to its internal energy. Thus the areal density variation is directly proportional to $\mathcal{E}_{hot}$:

$$\Delta(\rho R)/\rho R = -\mathcal{E}_{\rm hot}/\mathcal{E}_s.$$

The internal energy of a shell with the mass of 0.5 mg, the adiabat parameter $\alpha = 2$ and the density 10 g/cm^3 is 1.6 kJ. Thus the hot electron energy deposition of 0.5 kJ will reduce the areal density more than 30% while increasing the adiabat parameter by 50%. For the shell radius of 200 μm, the corresponding hot electron energy flux is ~ 100 kJ/cm^2 and the hot electron intensity ~ 0.3 PW/cm^2, supposing the spike duration of 300 ps. These numbers could be considered as the upper limits for the acceptable hot electron preheat level in the shock ignition fuel assembly.

3.2. Efficiency of shock ignition

Efficiency of shock excitation by the laser energy deposition is defined as a ratio between the energy of the shock $\mathcal{E}_{sh}$ and the laser absorbed energy $\mathcal{E}_{\rm abs}$. The deposited laser energy can be estimated as follows: the laser intensity that is needed to produce a pressure $p_{sh} = 300$ Mbar is defined from the scaling law (1). The absorbed laser intensity is ~ 4 PW/cm^2 for a wavelength of 0.35 μm. Considering that the target is compressed by a factor of 2 at the time of launching the spike, the radius of the ablation surface is $r_{\rm abl} \simeq 350\,\mu$m, [3], see also figure 1. Then the radius of the critical surface is almost twice larger, $r_c \simeq 550\,\mu$m, which corresponds to the critical surface of 3 mm^2. Then the absorbed spike power is ~ 125 TW and the laser spike absorbed energy is $E_{\rm abs} = 62$ kJ for the spike duration $t_{\rm spike} = 500$ ps. That corresponds to about 100 kJ of the incident laser energy assuming the absorption efficiency of 60%.

The energy in the shock wave can be estimated from knowing the shock pressure p_{sh} and the thickness of the shock front Δr_{sh}. Assuming the ideal gas equation of state with the polytrope parameter 5/3, the shock enthalpy is $5/2\,p_{sh}$ and the shock energy $E_{sh} = 10\,\pi r_a^2 \Delta r_{sh} p_{sh}$. The shock thickness can be estimated as a product of the sound speed in the ablation zone and the spike duration, $\Delta r_{sh} \simeq c_s t_{\rm spike} \simeq 50\,\mu$m assuming the acoustic speed of 100 μm/ns. Then the shock wave energy is about 3 kJ, that is the efficiency of shock drive is about 3% in the shock ignition conditions. The problem of shock hydrodynamic efficiency is one of the main issue in shock ignition physics.

The energy of hot spot at ignition $E_{hs} = 3\,M_{hs}T_{ig}/m_i$ depends on the hot spot mass M_{hs} and the ignition temperature $T_{ig} \simeq 8$ keV. The hot spot mass can be

estimated as $M_{hs} = (4\pi/3)\,(\rho R)^3/\rho^2 \simeq 3\,\mu$g for the hot spot density $\rho = 100\,\mathrm{g/cm^3}$ and the hot spot areal density of $0.2\,\mathrm{g/cm^2}$. Then the energy of hot spot needed for ignition is approximately 3 kJ. Moreover, the hot spot is already heated during the implosion stage up to the temperature about 2 keV. Thus, the shock needs to contribute of about 75% of the total energy, that is, 2.2 kJ. This estimate shows that the converging shock has to leave about 75% of its energy in the hot spot. This value is in agreement with the calculations of the converging shock energy deposition given in [52].

Concluding this section, we notice that the overall efficiency of the shock ignition scheme turns out to be rather low – of the order of 2% of the laser spike energy is deposited in the hot spot. However, the sequence of processes of energy transfer from the laser pulse to the hot spot are understood and controlled. The parametric instabilities and laser filamentation can affect the efficiency of laser spike coupling to the target. The laser power of 200 TW required for the shock launch is already available on the NIF facility. That opens possibility for full scale experimental test of the shock ignition scheme.

3.3. Symmetry of the ignition shock

3.3.1. Low mode irradiation asymmetry

The symmetry presents a serious challenge for shock ignition as for all inertial confinement schemes, although a relatively low implosion velocity provides a better control of the implosion process. Traditionally the small scale and large scale perturbations are considered separately. This is motivated by the difference in origin of the initial perturbations and in their theoretical and numerical analysis. As the perturbations for a spherical target can be developed in spherical harmonics, they are characterized by the orbital number l that present the number of perturbation wavelengths over the shell perimeter $\lambda = 2\,\pi R/l$. The low modes, $l \lesssim 10$ are due to inhomogeneity of laser irradiation and final number of incident laser beams. The high modes are due to the laser beam and target small-scale inhomogeneities.

The particularity of shock ignition is that the shock pressure is rather insensitive to the spike illumination asymmetry. This can be explained by the fact that at the moment of spike arrival the plasma corona is well developed, the distance between the absorption and ablation zones is about 200 μm, which allows an efficient smoothing of even low mode perturbations. To illustrate this effect, we consider the extreme case of the spike bipolar illumination [3]. The shock is launched by two laser beams arriving on the target along the polar axis. Figure 11 obtained in the 2D CHIC simulations shows the temperature and pressure distributions at three consequent stages. Just before the spike arrival, the temperature and pressure are uniform (left panel in figure 11). The temperature maximum corresponds to the position of the critical surface and the pressure maximum indicates the position of the ablation layer. The central panel in figure 11 corresponds to the rising part of the spike (~ 200 ps). The temperature and the pressure increase at the poles. That corresponds to excitation of the Legendre mode $l = 2$. However, 200 ps later the lateral electron thermal conduction reestablish the temperature and pressure symmetry (right panel in figure 11). The relative amplitude of the mode 2 at this moment is less than 10%. Thus even with a high irradiation laser asymmetry, the thermal smoothing allows to enhance the spike shock symmetry and still ignites the hot spot.

The "cloudy day" [53] model allows to evaluate quantitatively the stabilization

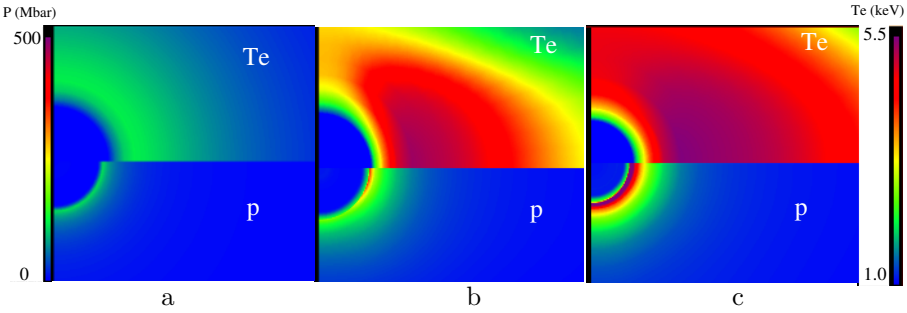

Figure 11. (Color online) Temperature (upper) and pressure (lower), before the power spike (a), during the spike laser rising up and 200 ps (b) and after the maximum of power spike (c). Simulation results are obtained with the radiation hydrodynamic code CHIC.

effect of the lateral heat transport. The pressure perturbation at the ablation front created by the fluctuations of the laser intensity reads:

$$\delta p_{\rm abl}/p_{\rm abl} = (2/3)(\delta I_L/I_L)(r_{\rm abl}/r_c)^l \tag{13}$$

where δI is the laser intensity perturbation. In the case of bipolar spike illumination $l = 2$, $r_c = 500\,\mu$m and $r_{\rm abl} \simeq 300\,\mu$m, then for a laser intensity perturbation of $\sim 50\%$, the ablation pressure perturbation is $\sim 10\%$. This order of magnitude of the pressure perturbation is in agreement with the 2D CHIC simulations shown in figure 11 and such a pressure perturbation does not prevent the hot spot ignition. However, the smoothing effect of the heat conductivity may be overestimated in these simulations as they did not account for the magnetic fields. As the temperature and the density gradient are not collinear, the magnetic field is generated and can modify the thermal conduction smoothing effect.

3.3.2. High mode hot spot asymmetry

The high modes are dangerous for the shell integrity. The growth rate of the Rayleigh-Taylor instability increases with the mode number, and the modes with wavelengths comparable to the shell thickness may rupture the shell. Moreover, the outer shell perturbations are transferred to the inner shell surface and are amplified during the deceleration and stagnation phase of the fuel assembly. These perturbations mix the shell material with the hot fuel inside thus reducing the hot spot volume and degrading the ignition conditions. The dominant mode number $l_* \simeq \sqrt{\pi N}$ can be estimated by knowing the number of laser beams N and supposing that they are distributed evenly over the target surface $4\pi R^2$. For example, in the HiPER project, where the target is supposed to be irradiated by $N = 48$ laser beams [55], the dominant mode is $l_* = 12$.

The advantage of the shock ignition scheme is that the Rayleigh-Taylor instability at the stagnation phase can be mitigated by the shock wave generated by the laser spike [3, 54]. Figure 12 shows the effect of the shock on the amplitude of the mode $l = 12$. In the case of standard implosion, figure 12(a), the mode is growing to a large amplitude in spite of thermal conduction smoothing. In contrast, the converging spherical shock wave decreases significantly the amplitude of the perturbation, figure 12(b). This effect can be explained by the differential acceleration of the inner shell surface. Similarly

to the Richtmyer-Meshkov instability, the density valleys experience an acceleration in the shock earlier that the density peaks thus reducing the instability growth rate. In the case of sufficiently strong shock the perturbation would be even reversed. Such a stabilization effect was observed in the planar experiments [56] and in the shock ignition experiment on the OMEGA facility [57]. In the latter case, it was found that the ratio of the measured neutron yield to the 1D predicted yield does not depend on the shell convergence, see Sec. 4.3.

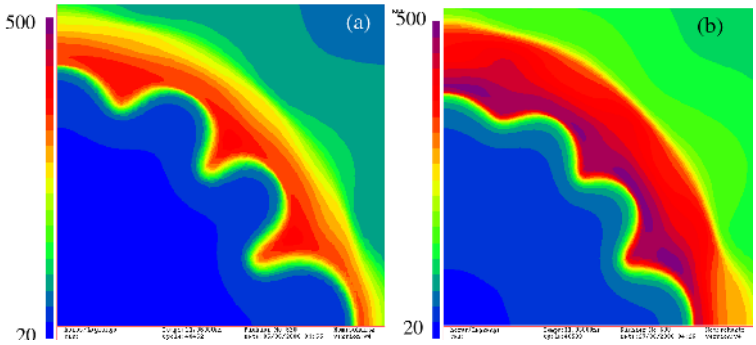

Figure 12. (Color online) Shell density distribution from the 2D CHIC simulation of the HiPER target at the time moment before stagnation [3]: the mode $l = 12$ for the case (a) without and (b) with the ignition shock (g cm^{-3}).

4. Experiments

4.1. Laser plasma interaction experiments

To be relevant to the shock ignition scheme, laser-plasma interaction experiments must be conducted in long and hot plasmas at high intensity. The plasma must contain all plasma densities up to the critical density with a typical inhomogeneity scale length of a few hundreds of microns. The geometry and the crossing beam effects must also be taken into account. These studies require multiple laser beams, to produce the plasma independently of the interaction beam(s), in the multi-kilojoule regime. A very limited number of such installations exists now all over the world, so it is necessary to design experiments on smaller laser systems that can address specific questions on the road to success of good laser-plasma coupling for shock ignition. As discussed in the introduction, the main questions concern the propagation and efficiency of the coupling of the shock ignition pulses in the plasma corona of the compressed targets. Past experiments have identified the most serious problems: filamentation, spreading and deviation of the laser beam which affect its propagation and intensity distribution, stimulated Brillouin and Raman scattering which can reject a large part of the incident laser energy outside the plasma.

4.1.1. Experimental conditions

To study these effects in complementary conditions, we have set up a program based on three laser installations: the six-beam LULI system (LULI-6F), 1 kJ LULI system (LULI-2000) and the LIL [58]. The first one has the advantages of driving multiple-beam irradiation that can be used to build sophisticated diagnostics and very well

controlled laser and plasma conditions with a complete flexibility and a large number of shots. The LULI2000 system provides a possibility to operate with two laser beams with energies $\sim$ 500 J. The LIL system delivers pulses on the 10 kJ level. The targets were chosen to emulate different parts of the density profile of the corona of a compressed target. Plasmas preformed from underdense foams and gas jets by the first laser beam were used to study the long low-density plasma. Their initial density was chosen to produce an electron density above or below quarter-critical density in order to evaluate the importance of mechanisms that can develop in this area, mainly absolute stimulated Raman scattering (SRS) and two-plasmon decay (TPD). Thick foils irradiated with the first laser beam were used to produce electron density profiles with the critical density. This is important for the growth of stimulated Brillouin scattering (SBS) in presence of reflected laser light as well as to study collisional absorption with high electronic densities.

Figure 13 summarizes the laser and plasma conditions that were used for these experiments with the LIL and LULI installations. The electron temperature up to 2 keV, the density gradient scale length up to 350 μm, the laser intensities up to 10 PW/cm^2 were obtained. Although it is clear that a short laser wavelength will be the most suitable for the shock ignition pulse, three laser wavelengths, 0.35, 0.53 and 1.05 μm, were used to reach high values of the main interaction parameter $I\lambda^2$. Different geometries of the laser beams with respect to the target were used to produce the plasma expansion in direction of the interaction beam or with an angle. This latter case was used to study the effect of beam steering and light deflection that can happen to the shock ignition pulses that are incident with an angle on the target.

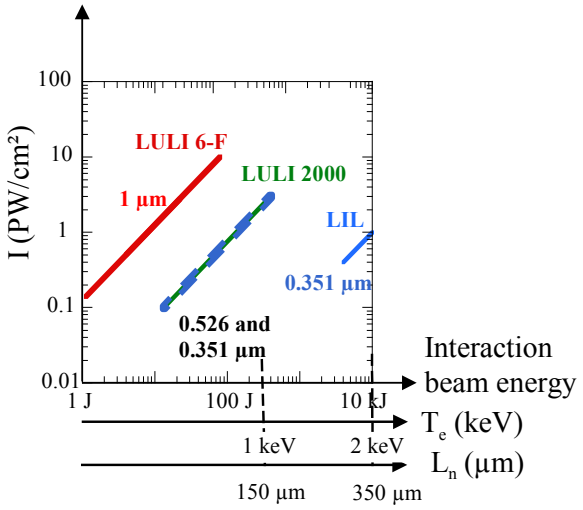

Figure 13. (Color online) Summary of the laser-plasma conditions for the interaction experiments in the context of shock ignition.

In this section, we present first results from experiments that demonstrate self-focusing, spreading, and beam steering of the interaction beam. Reflectivities due to SBS and SRS from long plasmas will then be discussed.

4.1.2. Laser beam propagation

All experiments at LIL and LULI have shown some laser beam spraying and plasma smoothing due to either forward SBS or filamentation when the laser power approaches the critical power. To illustrate this effect, we recall the 6-beam experiments, which had many diagnostics on the beam propagation mechanisms, but the plasma temperature was lower than expected under the shock ignition conditions. The laser interaction beam was diffraction limited, using a deformable mirror and a diaphragm, with a corresponding spot size measured at half-maximum of 21.5 μm. An example of the modification of the near field image of the laser intensity distribution after propagation through an underdense plasma compared to vacuum is shown in figure 14(a) as a function of time. The angular aperture of the incident beam was 6° as observed on the left panel of figure 14(a). It is widened by $\sim 50\%$ when going through a preformed plasma as one can see in right panel of figure 14(a). Figure 14(b) displays the 2D near field image, integrated over 100 ps, of the laser intensity at the output of the plasma at the time $t = 0.3$ ns. The light scattered outside the initial aperture cone is clearly observed. Spectral measurements of this light demonstrated that it was due to forward SBS. Broadening of the angular distribution of the forward scattered light was observed to increase with the plasma density but the results of this experiment were limited by the aperture of the collecting optics of the transmitted light.

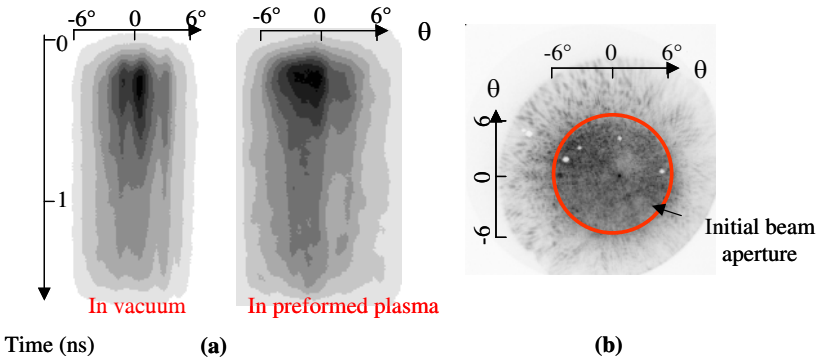

Figure 14. (Color online) a) Temporal evolution of the angular diagram of the transmitted light through an underdense plasma (right) compared to vacuum (left). b) Gated near field image of the intensity distribution at the output of the plasma at $t = 0.3$ ns.

Plasma beam smoothing, with weak beam spraying, was also observed in the LIL experiments using low-density foam plasmas [59]. These results were obtained in long and hot plasmas but the laser intensity was below what is expected for the shock ignition pulse. Plasma smoothing may be useful to control the SBS reflectivity to the condition that beam spraying does not affect too much the laser intensity in the critical region which must be high to produce the requested high-pressure shock. This effect must be different in spherical compared to planar geometry as, with multiple beams, the forward scattered energy from one beam could be added to the other beams.

Another important effect in the context of shock ignition is the oblique incidence of the shock pulse with respect to the density and expansion velocity gradients. Not only the laser beam will be reflected at plasma densities lower than the critical one

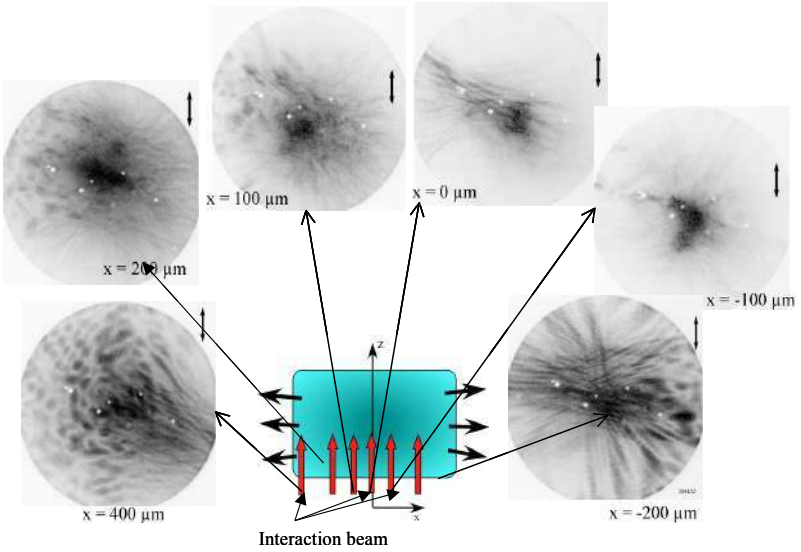

Figure 15. (Color online) Far field gated images of the intensity distribution of a laser beam incident at different positions on a transverse velocity profile. The experimental parameters are given in the text.

so that the high density regions could not contribute to collisional absorption, but also beam deflection and filamentation can happen to the rays that propagate in a flowing plasma [60]. To test these effects, a dedicated experiment was designed on the LULI-6F facility. The experiment used six laser beams with a special configuration to get the interaction beam axis perpendicular to the plasma flow. The plasma was created by two counter propagating 526 nm wavelength laser beams, ablating a 1.2 μm thick, 380 μm diameter CH disk, and heated by a third identical beam delayed by 900 ps with respect to the first two. The total power of the plasma forming beams was 0.2 PW/cm^2. The plasma was underdense, expanding rapidly along the preforming beam axis in two directions, backward and forward, with a parabolic density profile and a linear velocity profile. There was no plasma motion only at the top of the density profile. The high-intensity interaction beam, $I \simeq 1\,\mathrm{PW/cm^2}$, at the first harmonic, $\lambda = 1.053\,\mu$m was sent perpendicular to the principal plasma expansion axis at different positions along this velocity profile. The results are illustrated in figure 15 where far field-gated images of the intensity distribution inside the plasma are shown for various impinging positions on the transverse velocity profile. No breakup of the beam was observed when the laser impinges at the top of the plasma density profile where the flow velocity was almost zero. In contrast, a strong breakup happened in the case where the interaction laser beam propagated in a plasma with high transverse velocities. This is consistent with the modification of the filamentation threshold as a function of the transverse flow velocity and demonstrates that such an effect could have very deleterious impact on laser beams traveling at an angle in the corona of a compressed target. In the same experiment, beam steering was observed in the near field images.

4.1.3. Stimulated Brillouin scattering

SBS reflectivities have been measured in preformed plasmas for a large set of parameters with temporal and spectral resolution. Specific LULI-2000 experiments were designed to study SBS in long plasmas with two laser beams delivering nanosecond pulses. The plasma was produced by the irradiation of a thick $\sim 50\,\mu$m plastic foil with a first laser pulse of 1.5 ns and 300 J. The interaction beam was focused in this plasma, along the normal axis of the target, after a delay of 1.5 ns and a maximum intensity of $3\,\mathrm{PW/cm^2}$. The two beams were at the same wavelength, $0.53\,\mu$m in the first part of the experiments and $0.35\,\mu$m in the second part. Details on these experiments are reported in [62].

An example of time-resolved spectrum of the SBS light collected in the backward direction is shown in figure 16 together with its temporal evolution. A broad component that lasts around 150 ps is observed at the beginning of the interaction pulse. It is followed by a narrow component that moves towards shorter wavelengths. The spectra were interpreted by the formation of a velocity plateau in the high-density region early in the interaction pulse, which then moves towards lower densities explaining the blue shift of the SBS spectrum. The plateau formation may results from the increased ablation rate when the interaction beam is fired after the creation phase. This may happen in the case of shock ignition as the shock pulse must have an intensity well above the compression pulses. Most of the SBS spectra were blue-shifted, which combined with hydrodynamics simulations of the density and velocity profiles, gives information about the location of the SBS activity. It indicates that SBS grows in the low-density part of the profile. The absence of SBS activity in the high-density region was interpreted by the effect of filamentation and self-focusing of the beam in the highest density region with significant beam spray resulting in reduced beam temporal and spatial coherence.

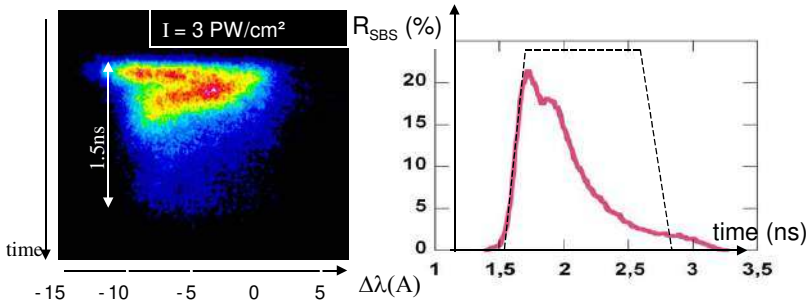

Figure 16. (Color online) a) Time-resolved spectrum of the backward SBS light in the $2\,\omega$ experiment at an intensity of $3\ \mathrm{PW/cm^2}$. b) Temporal evolution of the SBS reflectivity. The laser pulse shape is shown with the dotted line.

We have studied the evolution of the backward time-integrated reflectivities as a function of the laser intensity and observed the growth and saturation of SBS. An interesting result was that the saturated backward reflectivities were in the same range, $\sim 10\%$, both for $0.53\,\mu$m and $0.35\,\mu$m laser wavelengths [59]. This 10% level is similar to what was observed previously in $1.05\,\mu$m experiments at intensities up to $10\ \mathrm{PW/cm^2}$ with the LULI-6F facility.

A too quick conclusion would be that the SBS reflectivity does not look to be

an issue as one can afford 10% losses. Three important observations complete these results:

- the duration of the SBS emission is shorter than the laser pulse;
- a significant amount of scattered light was collected outside the focusing optics;
- the location and the extension of the plasma area where SBS grows change with the laser intensity.

The near back scattering was measured in an aperture twice the incident optics, and is shown in figure 17. Typically, at high intensities, the same amount of light was scattered outside than inside the focusing optics. This brings already the SBS reflectivity to twice the initial value.

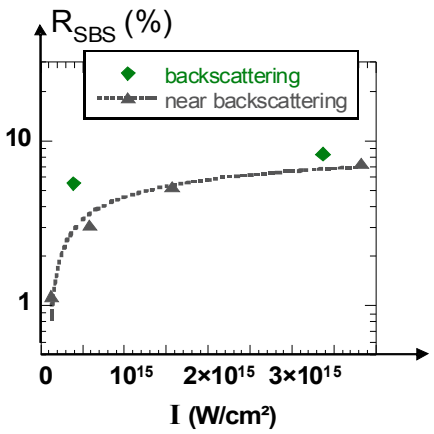

Figure 17. (Color online) Time-integrated SBS reflectivities measured at 2ω including backscattering and near backscattering measurements.

In all three experiments, the six-beam, the LULI-2000 and the LIL, we have observed that the SBS reflectivity, at high intensity, is always shorter than the interaction pulse duration and SBS grows at the very beginning of the laser pulse. This is shown in figure 16(b) and figure 18 and it corroborated with the numerical simulations presented in Secs. 2.2 and 2.3. This means that the average reflectivities measured with laser pulses in the nanosecond range are not meaningful for the shock ignition pulse which will have a duration of a few hundreds of picoseconds. For a SBS duration of one third of the total laser pulse, reflectivities for the few first hundreds of picoseconds would be ~ 3 times larger than the average reflectivities.

Beside the new experiments conducted recently, one has to reconsider carefully all previous results obtained on the SBS in the last forty years. Past experiments have demonstrated that the size of the SBS emitting volume increases with the SBS reflectivity [63]. It has been also shown that a few small regions of plasma contribute to SBS and that SBS reflectivity from these regions is $\sim 50 - 100$ higher than the average SBS reflectivity [64]. This is consistent with the results from Ref. [65] where it was observed that the IAW saturation amplitude is independent of the density, and the total SBS reflectivity increases with the width of the saturated spectrum thus showing instantaneous values of $\sim 50\%$. Seeding SBS may also affect its nonlinear saturation [66]. In the case of crossing beams, SBS may be seeded by reflections or

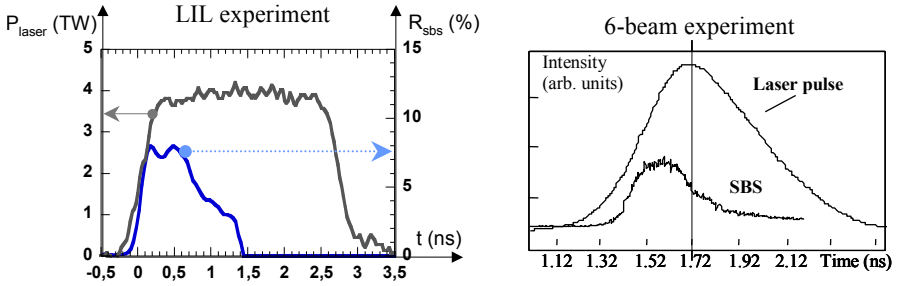

Figure 18. (Color online) Temporal evolution of the backward SBS reflectivity in the LIL (left) and in the LULI-6F (right) facilities.

shared ion acoustic waves [67]. Finally, taking everything into account, it is most likely that SBS reflectivities could be very high for the shock ignition pulse conditions. To avoid this problem, all possible beneficial effects that could reduce the SBS emission like beam and plasma smoothing, target composition, aperture of the optics must be considered.

4.1.4. Stimulated Raman scattering

In most of our experiments the stimulated Raman scattering reflectivity stays at low level, typically below or around a few percents. The contribution of the quarter-critical density in the Raman spectra has always been negligible compared to SRS coming from lower plasma densities. We have found high levels of SRS only in gas jets where it could grow in the absolute regime until saturation at a level of around $20-25\%$ depending on the plasma electronic density [68]. Three results are of interest in the context of shock ignition as they give tendencies on how the SRS growth could evolve with interaction conditions:

- the effect of the density scale length on the Raman reflectivity;
- the effect of laser intensity on the SRS spectra;
- the effect of plasma length on the SRS reflectivity.

The LIL installation, with square pulses of typically 12 kJ of $3\,\omega$ light and 2.7 ns duration, was used to produce long and hot plasmas from foam targets with very small ($\sim 1\,\mu$m) cell structures. The maximum average intensity on target was $8\times10^{14}\,\mathrm{W/cm^2}$. Temporal smoothing was achieved by means of the chromatism of the focusing grating which creates a longitudinal dispersion with a spectral broadening introduced in the laser source by an electro-optic modulator. Various initial foam densities, between 3 and 10 mg/cc (respectively 10% and 35% of the critical density for $3\,\omega$ light) were used. The foams length has been varied from $300\,\mu$m to 1 mm. In all cases, because of the long pulse duration, some plasma expanded toward the laser, so that, after a few hundreds of picoseconds, the density profile displayed two parts: an increasing electron density in the front and a plateau at an electron density determined by the initial foam density in the backward parts of the plasma.

Using relation (10), the time-resolved spectra of the backward SRS light were used to determine the location and the extension of the SRS emitting region of plasma as a function of the interaction conditions. For 3 mg/cc foams, the SRS spectra were quite narrow and limited by the low electron density that could be produced ($\lesssim 0.1\,n_c$).

Using 7 and 10 mg/cc foams, we observed that the width of the SRS spectra increased with the initial foam density showing that Raman could grow on a larger density range. The level of SRS reflectivity increased accordingly. The Raman evolution as a function of the density scale length of the plasma expanding in the front part was deduced from the analysis of the Raman intensity as a function of time in 10mg/cc foams. The scale lengths were deduced from the hydrodynamics CHIC simulations. Results are reported in figure 19(a), showing an increase of SRS from 3 to 5% for scale length increasing from 150 μm to 350 μm for a laser intensity of 0.4 PW/cm^2. However, the estimated gain factor (5) varies in from $G = 0.5$ for the scale length of 150 μm to $G = 2$ for the maximal one. These scale lengths are well in the range of those that will be encountered by the shock ignition pulses, but the laser intensity is lower so that the low observed SRS levels may not be representative of what could happen in shock ignition conditions.

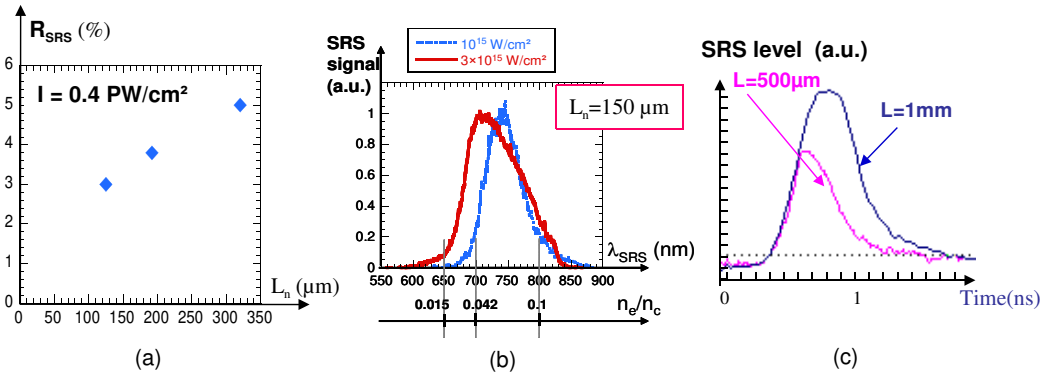

Figure 19. (Color online) a) SRS reflectivity as a function of the electron density scale length (LULI-2000 2 ω experiment). b) SRS spectra for two laser intensities (LULI-2000 2 ω experiment); c) Effect of the plasma length on the SRS reflectivity as a function of time (3 ω LIL experiment).

To study the effect of the laser intensity, we have performed experiments with the LULI2000 installation using the same foams as in the LIL campaign. The laser was at 2 ω with 400 J in 1.5 ns. The main result was that the SRS spectra were widened towards short wavelength when the laser intensity increased. This means that SRS extends to lower plasma densities at higher intensities, eventually to area where the Landau damping parameter $k\lambda_D$ is quite high. An example of such spectral modification presented in figure 19(b) shows that the minimum plasma density relative to critical density where SRS activity is observed extends from 4.2 to 1.5% when the laser intensity is increased from 1 to 3 PW/cm^2.

The effect of the plasma length on SRS reflectivity was studied in the LIL experiments. As shown in figure 19(c) for foam with initial density of 7 mg/cc and a laser intensity of 0.6 PW/cm^2, the SRS reflectivity increases with the initial foam length, from 0.5 to 1 mm, and had a longer temporal duration, demonstrating an effect of the plasma corona extension.

Although the observed SRS characteristics are in general in agreement with the simulations presented in Sec. 2.2, it is too early to draw conclusion on SRS in shock ignition conditions. The observed tendencies as a function of the density scale length,

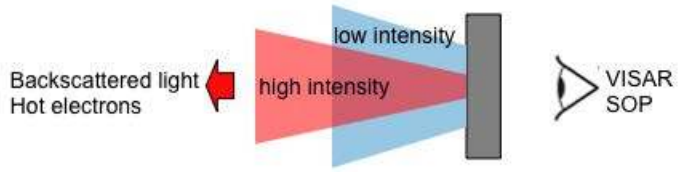

Figure 20. (Color online) Principle of the experimental set-up for the planar shock experiments.

the laser intensity and the plasma length, indicate some possible problems with Raman losses for interaction conditions of the shock ignition scheme.

4.2. Planar shock experiments at LULI, PALS, and OMEGA

As the shock ignition scheme is relatively new, only few experiments dedicated to the shock formation have been conducted up to now, while more and more numerical simulations were widely performed recently. In particular, it is important to study the laser plasma interaction and a high pressure shock formation in the same experiment in order to evaluate the efficiency of hydrodynamic coupling and compare the data with the simulations. This is the key point in validation of the shock ignition concept. In this context, the experiments have been performed in the planar and spherical geometries. This section presents the results of planar experiments performed at LULI, PALS and OMEGA laser facilities, while the following section will be focused on the spherical implosions conducted at the OMEGA facility.

4.2.1. Experimental parameters

The planar geometry is not completely adequate for studying shock ignition as the convergence effect cannot be reproduced. However, it is extremely favorable for detailed measurements of the spike generated shock correlated to the level of parametric instabilities. The large number of diagnostics, compatible with the planar geometry, turned out to be particularly useful for accurate comparison with numerical simulations and to constrain them, giving confidence in more complex cases where the implementation of diagnostics is more difficult.

While the three laser facilities differ in their capabilities, the experiments performed at LULI [69], PALS [70, 71] and OMEGA [72] are all based on the same principle, as shown in figure 20. The targets were irradiated by a laser pulse consisting of two parts: The first one, the plasma creation pulse, was at low intensity in the range of $0.01 - 0.2\,\mathrm{PW/cm^2}$. It launches the first shock into the target and creates a large coronal plasma reminiscent of a shock-ignition environment. The second part provides the high-intensity spike at an intensity of $1-10\,\mathrm{PW/cm^2}$ that launches a second strong shock into the target. While the principle idea behind the experimental campaigns at each facility was the same, the experimental details were varied.

Both experiments at LULI and PALS employed one laser beam each for the low- and high-intensity part, whereas the experiments at OMEGA comprised a total of twenty beams overlapped at the target to generate the intensity profile. At LULI, the two beams were at $2\,\omega$ (wavelength $0.53\,\mu\mathrm{m}$), whereas the wavelength at OMEGA was $0.35\,\mu\mathrm{m}$ ($3\,\omega$) and at PALS, $1\,\omega$ for the plasma creation beam and $3\,\omega$ for the spike

beam. Note that PALS is an iodine laser, so the first and third harmonics correspond to wavelengths 1.33 μm and 0.44 μm, respectively. The irradiation at 1 ω for the first beam was chosen with the goal of maintaining a sufficiently high temperature despite the low intensity available in the creation beam. The pulse durations were 2 ns for each beam at LULI, and 300 ps at PALS. On OMEGA, a succession of three pulses of $\sim$ 1 ns was used with 0.5 ns temporal overlap between the last two pulses. This created a shaped pulse with a low intensity foot of 1 ns duration, followed by a higher intensity 0.5 ns plateau pulse and a subsequent 0.5 ns high intensity spike.

In all experiments, to reach the necessary high intensities, the spike beam was focused to a smaller focal spot (Ø$\sim$ 100 μm for LULI and PALS, and Ø$\sim$ 600 μm for OMEGA) than the plasma creation beam (Ø$\sim$ 400 μm for LULI, Ø$\sim$ 900 μm for PALS and Ø$\sim$ 900 μm for OMEGA). At PALS and LULI, phase plates were used in the creation beam, in order to produce a large scale and relatively uniform plasma. In contrast, the spike beam, was not smoothed in order to get a smaller spot and higher intensities. On OMEGA, polarization smoothing and distributed phase plates were implemented in 14 pre-plasma generating beams, while small-spot phase plates were implemented in 6 high intensity spike beams. The energy contained in the spike beams was varied to give an overlapped spike intensity ranging from 0.5 to 1.5 PW/cm^2, while keeping the pre-plasma conditions the same throughout the experiment. The main parameters are summarized in table 1.

	Creation plasma pulse				Spike pulse				Delay
	λ μm	τ ns	Ø μm	I PW/cm^2	λ μm	τ ns	Ø μm	I PW/cm^2	Δt, ns
LULI	0.53	2.0	400	0.07	0.53	2.0	100	1.0	$1-2.4$
PALS	1.33	0.3	900	0.01	0.44	0.3	100	10	$0-1.2$
OMEGA	0.35	1.5	900	0.2	0.35	0.5	600	$0.5-1.5$	1.5

Table 1. Experimental parameters for the planar shock experiments.

Since two beams were totally independent at PALS and at LULI, it was possible to vary the delay between the plasma creation beam and the spike, thus changing the plasma density scale length. By studying the delay dependence of the reflectivity, hot electron production, and the shock velocity we are able to estimate the influence of the plasma parameters on the level of parametric instabilities and on laser absorption efficiency.

The target design and the suite of diagnostics were very similar at LULI and OMEGA. The targets consisted of multiple layers, with a plastic (CH) layer on the laser side mimicking a low-Z ablator of real ICF pellets. This layer absorbs the incident laser light, while minimizing the X-ray production that might preheat the target. The second layer made of a high-Z material (copper or molybdenum) was used to block X-rays from the front side of the plasma. It also served as a fluorescence layer to diagnose fast electrons that were generated through parametric instabilities, via Kα emission. The third target layer made of an α-quartz, was used as a witness layer where the shock dynamics could be observed using the VISAR diagnostic. For the PALS experiment, the third layer was made of aluminum, since only the streaked optical pyrometer (SOP) for shock chronometry was available. The mean shock velocity was measured either with VISAR by using targets with a step on the rear side, or with SOP by measuring the time between the laser arrival at the target front (through an optical time fiducial) and breakout at the rear of flat targets.

Although each of these experiments has its specificities and limitations, they

are complementary and demonstrate a capacity to launch a strong shock in a large pre-plasma. Relatively small focal spots for the spike beam used at the LULI and PALS installations result in stronger two-dimensional (2D) effects, which complicate comparisons with numerical simulations. The OMEGA experiment used significantly larger spots, which mitigates 2D effects, even though they are still present and were taken carefully into account in the data analysis. Although the duration of PALS beam matches well the required spike time, the energy of creation beam is too low to heat the pre-plasma to the keV temperatures expected in fusion targets. Moreover, the shock pressure was decreasing after the spike end, which implies the need for detailed numerical simulations connecting the measured (lower) pressure at shock breakout to the initial one created by the laser pulse. The intensities reached at PALS of up to $10\,\mathrm{PW/cm^2}$ are also interesting for studying the parametric instabilities in laser and plasma conditions that are not yet well known. A particular effort to diagnose precisely the plasma conditions has been conducted on PALS. This includes the high resolution X-ray spectroscopy [73] measuring the emission lines of chlorine dopant included in the plastic layer, the optical interferometry and a new diagnostics of plasma density based on the X-ray deflectometry [74].

4.2.2. Spike pulse reflectivity

In all experiments, a large set of diagnostics has been implemented (most of them are the same on the three experiments) to estimate, simultaneously:

- the backscattered energy of the spike (time-resolved SBS and SRS reflectivities as well as time-resolved spectra);
- the hot electron production;
- the shock velocities.

The reflectivity due to the parametric instabilities driven by the spike beam as it propagates through the large plasma have been measured. Figure 21 summarizes the measured total plasma reflectivity (SRS and SBS) within the laser beam cone obtained from three laser facilities. The backscattered fraction of light is relatively low at LULI (the total reflectivity, corresponding to the SBS and SRS, is limited to 12% at maximum). At PALS, the total reflectivity was even lower (possibly due to the shorter wavelength), always below 5% in all cases and mainly dominated by SBS. The scattered light outside the focusing cone was measured with a few calorimeters and was about of the same order of that within the cone lens, bringing the total reflectivity to $\lesssim 10\%$. Secondly, variation of the delay between two beams, that is, the plasma density scale length, did not affect the backscattered energy in the PALS and LULI experiments. This appears surprising because the conditions of interaction are expected to change dramatically. In contrast to the PALS and LULI results, a strong increase in the plasma reflectivity with the spike intensity was measured on OMEGA. However, for planar targets and intensities of up to $1.5\,\mathrm{PW/cm^2}$, a total reflectivity within the focal cones of up to 6% was measured, which is lower than in the LULI and PALS experiments. This may be explained by multiple overlapping beams equipped with distributed phase plates used on OMEGA. Lower plasma reflectivity and better coupling is expected for smoothed laser beam profiles.

Another set of experiments were performed with spherical targets, which is discussed in more detail in the following section 4.3. In those experiments, tightly focused beams were directed onto an imploding plastic shell target. Most of the shots

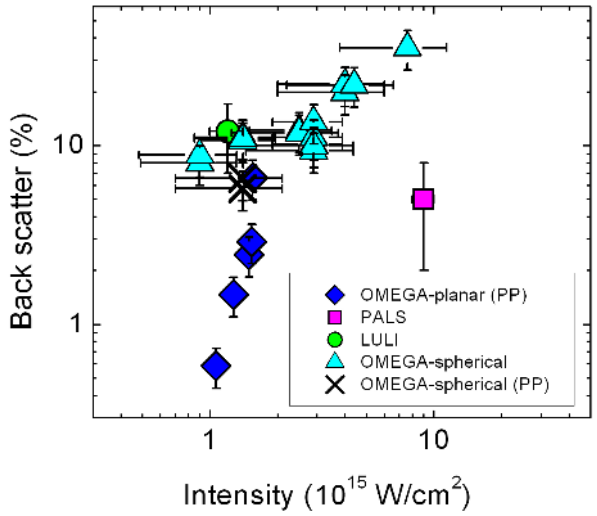

Figure 21. (Color online) Reflectivities in percent of the spike beam within the focusing cone as function of the spike intensity. The circle and the square represent the total reflectivity from the LULI and PALS experiments, respectively, while the diamonds (planar targets), the triangles (spherical shells), and the crosses (spherical shells, with phase plates) are from OMEGA. The data from spherical imploded plastic shells are discussed in Sec. 4.3.

were performed without beam smoothing in the spike beams (triangles) and only a couple of shots were performed with small spot phase plates (cross). As expected, better coupling is achieved with phase plates and a back reflection of a few percent in the $\sim 1\,\mathrm{PW/cm^2}$ range was measured for both planar and spherical targets. Without phase plates and intensities reaching $\sim 8\,\mathrm{PW/cm^2}$, the reflectivity strongly increased up to 36% (triangles), which is significantly higher than the PALS results. Although a general trend of increasing reflectivity with the spike intensity is seen in figure 21, the differences between the experiments are not fully understood. They may be due to differences in the target geometry and the laser wavelength.

OMEGA experiments showed a strong increase in SRS reflectivity with intensity and SRS dominated the back scatter signal at the highest intensity [34]. Only a modest increase in SBS reflectivity was observed with intensity. The SRS data are in agreement with numerical simulations presented in Sec. 2.2 that also predict a large SRS signal [32]. In the spherical target experiments, almost all of the backscattered light was detected within the cone of the laser beam with very little side-scattering. This is attributed to the strong interaction of single high intensity beams with the plasma corona creating a channel through the under-dense plasma up to the critical density, which guides back reflected laser light within a certain solid angle. In contrast, the planar OMEGA experiments were performed with multiple overlapping beams where channeling is not of importance and side scattering was significantly higher. Preliminary analysis indicates that a few percent of the laser energy is scattered outside of the laser cone.

Figure 22 shows an example of Raman backscattered spectra obtained at PALS for three delays. According to the formula (10) from the SRS spectral shift, the recorded scattered light spectrum in the range from 680 to 720 nm (FWHM) corresponds to

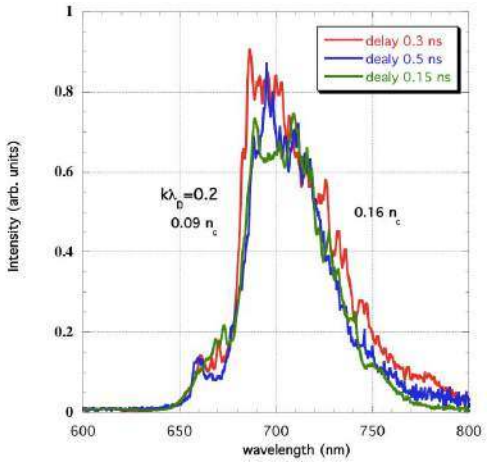

Figure 22. (Color online) Backscattered Raman spectra obtained at PALS at different pre-pulse delays.

plasma densities between 0.09 and 0.16 n_c. No sign of emission from the layer at $n_c/4$ is obtained, and the spectrum does not depend on the time delay between two laser pulses. These features could either indicate a strong absorption in the plasma corona or the spike beam filamentation and cavitation as that predicted in Ref. [36], see also Sec. 2.3. These processes could partially decouple the spike beam from the dense plasma implying generation of a lower pressure shock.

4.2.3. Hot electron generation

Hot electrons, which are principally generated by parametric instabilities such as SRS and TPD as it is discussed in Sec. 2.1, are an important element of the shock ignition scheme. They might be either beneficial and increase the strength of the shock wave or they are detrimental and lead to preheating of the compressed capsule. This depends essentially on the energy of these electrons and the time when they are generated. Careful characterization of the hot electron population is therefore required and has been inferred from Kα spectroscopy and X-ray diodes in these experiments. The planar target experiments on OMEGA show a conversion efficiency of 2% of the spike beam energy into hot electrons and temperatures of $\sim$ 70 keV at the highest intensity [72]. The numbers are inferred from spectroscopy of the Mo Kα emission from a diagnostic layer using an absolutely calibrated spectrograph and a time resolved multi-channel hard X-ray detector. Both, the hot electron number and the temperature increase with laser intensity. It is interesting to note that in the spherical OMEGA experiments significantly lower temperatures around 30 keV were measured [34]. Comparison of these data with numerical simulations discussed in Secs. 2.2 and 2.3 indicates that SRS is the primary generation mechanism and TPD is significantly suppressed.

The results obtained from Kα emission at LULI are partial because only very energetic electrons with energy higher than 60 keV were able to reach the second layer and to excite Kα. The Kα signal was found to be always below the noise level, giving an estimation of a very low laser light fraction converted into hot electrons above 60 keV. This result is consistent with the measured weak value of SRS reflectivity and

with the numerical simulations presented in Sec. 2.2.

The results on hot electrons at PALS were obtained from Kα emission by using both a single-hit CCD and a Kα imager based on a spherically bent crystal and a CCD detector. The energy of fast electrons was estimated by using targets with a plastic layer of different thickness. From the decay of Kα signal with the target thickness the average energy electron was evaluated to be ~ 50 keV. The total number of fast electrons was low with a conversion efficiency of laser energy to fast electrons of at most 1%. This is consistent with the low measured level of parametric instabilities.

4.2.4. Shock pressure measurements

The measurements of the shock velocity are particularly important because they provide an accurate estimation of the shock pressure and hence of the overall coupling efficiency, that is, the energy conversion from the laser beam to the shock. There are two ways for measuring shock velocity: the instantaneous velocity at the rear side from a VISAR diagnostic (employed at LULI and OMEGA), and the mean velocity, by using step targets (PALS) and comparing relative propagation times through the targets of different thicknesses.

The measurements of shock breakout recorded on the three facilities have been compared with 2D hydrodynamic simulations, as well as the instantaneous shock velocity obtained from the VISAR diagnostic at LULI and OMEGA. Pressures are deduced from the measured shock velocity coupled to tabulated Sesame equation-of-state (EOS) [75]. In all cases, the pressure created by the spike is found to be lower than the expected ablation pressure using the nominal on-target intensity and the formula (1). This emphasizes that knowledge of the absorbed laser energy is crucial in the shock ignition scheme, and laser coupling with the large pre-plasma has to be studied very precisely. As it was discussed in Sec. 3.1, the expression (1) for the ablation pressure is based on simplified assumptions, such as localized collisional laser absorption near the critical density. It is therefore not expected to fully capture the absorption physics. A good agreement between experiment and simulations is obtained for LULI and OMEGA. The experimentally estimated pressure as well as the different events during the propagation of the spike shock (coalescence and shock breakout) are well reproduced in simulations.

Figure 23(a) presents a typical image obtained from the VISAR diagnostic on the LULI experiment. On this time-resolved image, one can clearly observe the breakout of the first shock at the Ti-SiO_2 interface and the coalescence between the first shock generated by the creation plasma beam and the strong shock launched by the spike beam. The delay between two beams is 1.7 ns and the coalescence corresponds to the time when the shock driven by the spike beam catches up with the shock of the first beam. The velocity profiles as the function of time obtained from the measured data and numerical modeling are shown in figure 23(b). A good agreement between experiment and simulation for the first four nanoseconds allows estimating correctly the pressure of the spike shock, which is, in these conditions, of around 40 Mbar in CH.

The 2D effects arising from the small focal spot size of the spike beam at LULI have been carefully considered. Despite the larger focus in the OMEGA experiments, 2D effects are also important and were considered in the modeling. Concerning the pressure, from the 2D simulations, the pressure of the spike is around 40 Mbar in the LULI experiment, which is in agreement with the shock velocity measured in the experiment [69]. This pressure is in agreement with Eq. (1) if the absorption

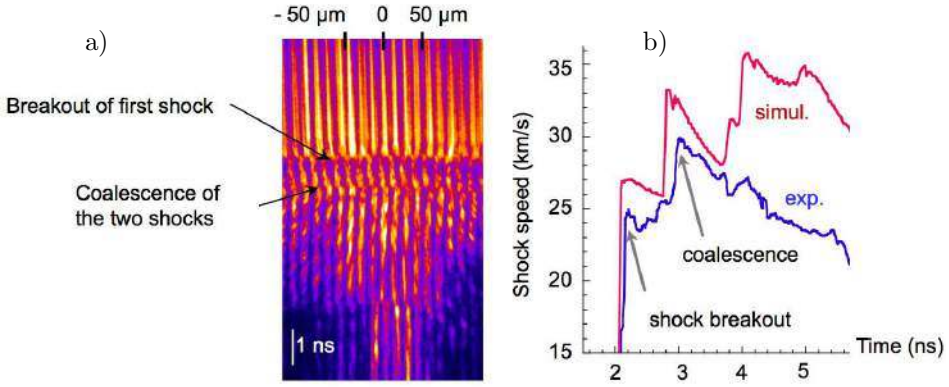

Figure 23. (color online) a) VISAR image recorded for a delay of 1.7 ns between the two beams. Laser beams irradiate the target from the top side of the figure and the time goes down. b) Velocity profiles as the function of time corresponding to panel a) from measured data (blue) and numerical modeling (red).

coefficient of the order of 60% is accounted for. It is essentially due to the collisional absorption in the LULI conditions. Similar results were obtained on OMEGA. Here, the obtained pressure was higher and reached up to 70 Mbar for a peak intensity of 1.5 PW/cm^2 in the planar geometry [72]. Excellent agreement, better than 5%, between the measured and predicted shock breakout times was obtained. Based on the comparison of inferred pressure and predicted pressure from a simple model (1), the coupling of the laser energy into the plasma is estimated between 60 and 80%, slightly higher than in the LULI experiment.

Comparisons of experimental data with simulations for the PALS experiment are more difficult due to stronger 2D effects linked to the small focal spot and the short duration of the spike. Both effects are not favorable for maintaining the shock. Those factors can contribute to explain a larger discrepancy observed between experimental results and simulations. At PALS, the experimentally observed shock velocity at the rear side of the target is compatible with an initial shock pressure, generated by laser-matter interaction at the target front, of about $\sim$ 90 Mbar. Although this is the highest pressure measured in these three experiments, it is significantly lower than what is expected on the basis of Eq. (1). Such a difference can be explained either as a result of filamentation taking place in the plasma, spreading the beam and reducing the effective on-target intensity, or due to the collective processes that are governing energy transport and shock formation. These effects have been already discussed in Sec. 4.1.2. The filamentation threshold [18] is certainly exceeded in all three experiments. A precise evaluation of such a threshold is however quite difficult because the spatial quality is the spike beams was not well controlled. When phase plates were not used (in order to achieve the required intensities), the laser beam focal spot contains hot spots with significant variations of intensity from point to point, that are difficult to predict, especially if one consider their evolution during propagation in the plasmas. It is even more difficult to evaluate the impact of filamentation on beam spreading. Therefore, more experiments with better characterized more energetic laser beams and better beam smoothing are required. Additional modeling efforts are

needed to study the impact of hot electron transport and the self-generated magnetic fields on shock formation.

Nevertheless, the first results from planar experiments are encouraging. Spike generated peak pressures of up to $\sim$ 90 Mbar are inferred from the measured shock velocities. Although this is not yet as high as needed for shock ignition, interesting physical effects are emerging. Special efforts to diagnose more precisely the propagation of high intensity laser beam in the large pre-plasma and a more complete study on fast electron production and transport should be conducted in order to evaluate the validity of shock ignition is a viable ICF alternative scheme.

4.3. Shock ignition implosions at OMEGA

Shock ignition separates the fuel assembly phase from the ignition phase by compressing a massive capsule on a low adiabat ($\alpha \sim 1$) using a low implosion velocity ($u_{\rm imp} \lesssim 300\,{\rm km/s}$). The ignition phase is initiated by launching a strong ($\sim 300\,{\rm Mbar}$) shock in the interaction region. The shock increases in strength while propagating through the imploding and converging shell leading to a non-isobaric hot spot. One way to generate a strong shock is by adding a high power laser spike at the end of the drive pulse. The OMEGA facility has the capability that allows us to investigate important physics issues of the shock ignition scheme using surrogate implosions. This includes questions of how a power spike at the end of a drive pulse affects the hydrodynamic stability of the shell and what effect it has on the shell compression and the hot spot compression.

The relative effect of the shock can be investigated by comparing the implosion performance with and without spike. OMEGA spherical shell experiments also address the sensitivity of implosion to laser-plasma instabilities during the high intensity spike. The experimental campaigns of imploded spherical shells on OMEGA provide first demonstrations of the feasibility and advantages of the shock ignition scheme. Two approaches have been pursued in the recent years: 60-beam symmetric implosions that use the same pulse shape with a late power spike on all 60 beams (that demonstrated an improvement in the neutron yield and in target compression) and a configuration that uses 40 low intensity beams for compression and 20 high intensity spike beams for shock generation in laser plasma interaction studies. The latter approach allows one to increase significantly the single-beam spike intensity and to evaluate their effect on the hydrodynamic performance and their role on laser plasma interaction processes at laser intensities that are relevant for shock ignition. This approach is also relevant for shock ignition designs on NIF [2, 4] or LMJ [5], where composite irradiation schemes are under study [76, 77]

4.3.1. Symmetric 60-beam implosions

Plastic shell targets filled with deuterium gas, see figure 24(a), are convenient to study basic physics issues of the SI concept in terms of the correct timing of the spike shock wave (SSW) and the rebound shock wave from the target center [57]. This is crucial for SI since the concept relies on a proper timing of both shocks in order to obtain a non-isobaric fuel assembly in the core that is necessary for ignition. Experiments were performed with $40\,\mu$m thick shells covered with a thin Al layer and with an outer radius of $\sim 430\,\mu$m. The shell were filled typically with $\sim 25\,$atm of D_2 gas. The implosion performance was optimized by varying the timing of the front picket pulse and the late power spike see figure 24(b). We concentrate here

on the timing of the spike. Figure 25 shows the measured neutron yield for a series of implosion with various spike onset times. Data is included for two picket timings. Most of the shots were performed with ~ 17 kJ of laser energy and only two shots were done with higher energy, as indicated in the figure. Maximum yield was obtained with an implosion with a 2.8 ns spike delay and 18.6 kJ of laser energy that performed better than an implosion without spike and laser energy of 19.4 kJ. This demonstrates that with proper timing, SI implosions lead to significantly improved neutron yield. The neutron and proton yields are respectively four and five time higher.

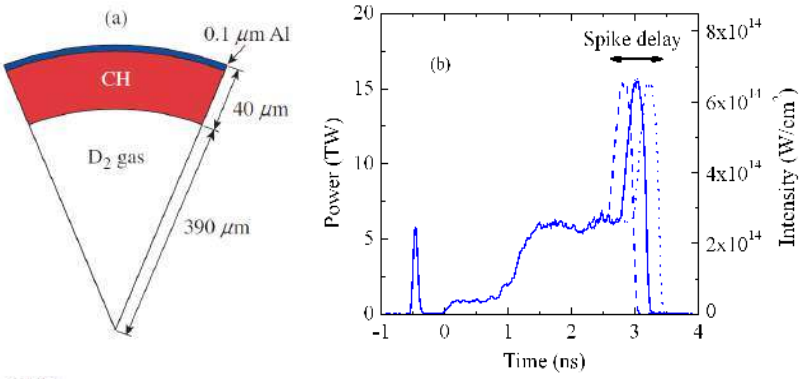

Figure 24. (Color online) a) Warm plastic shell used on the first SI 60-beams implosions. b) Typical SI pulse shape with a variable spike delay.

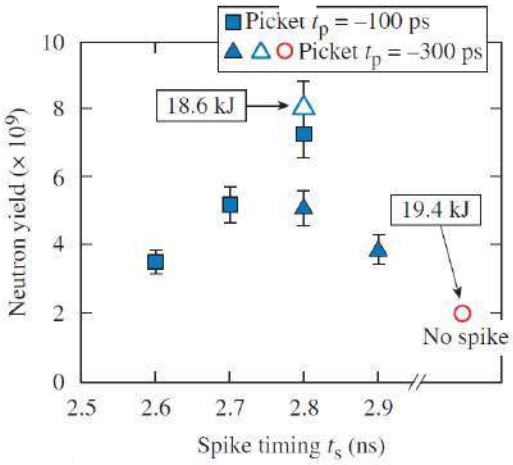

Figure 25. (Color online) Measured neutron yield as a function of the onset of the spike pulse [57]. Reproduced with kind permission of the American Institute of Physics.

These enhanced performances were not expected based on 1D yield calculations, which only predicted a 30% yield enhancement by the spike for our conditions. A survey study was performed at the optimum timing for a range of convergence ratios (CR) of the implosions, which was changed with the shell-fill pressure (from 7 to

30 atm). The convergence ratio is calculated and is defined as the initial inner radius of the target shell divided by the minimum radius of the gas-shell interface at peak compression. The CR increases with lower fill pressure. The ratio of the measured to the 1D predicted neutron yield, the yield-over-clean (YOC), is significantly higher in surrogate SI implosions compared to standard implosions, see figure 26(a). In the standard implosions without spike the YOC decreased by a factor of 4 down to $\sim 1\%$, when CR was increased from ~ 11 to ~ 23, which suggests an increased small-scale mixing for smaller hot-spot radii. In comparison, implosions with spike demonstrate a YOC close to 10% indicating that mixing of cold shell material into the hot spot was mitigated.

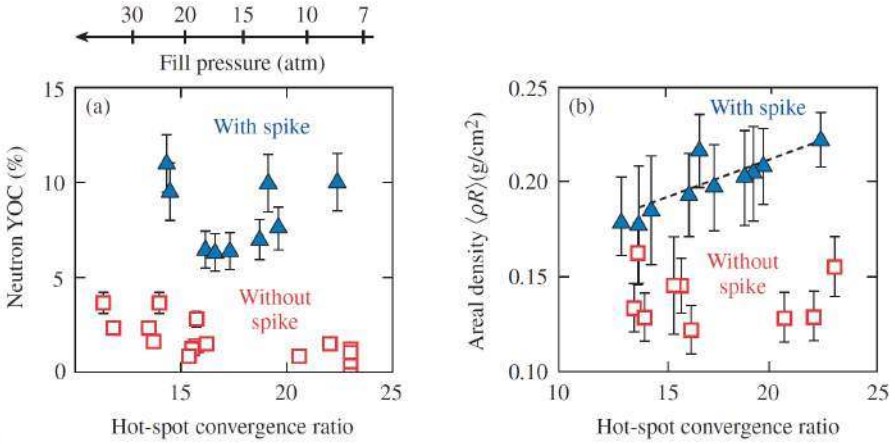

Figure 26. (Color online) a) The neutron yield-over-clean and b) the measured areal density versus 1D calculated hot-spot convergence ratio [57]. Reproduced with kind permission of the American Institute of Physics.

The higher stability of the shell implosion is also confirmed by the small standard deviation of areal density measurements from the different lines of sight. Neutron rate averaged areal densities, ρR, of the order of $200\,\mathrm{mg/cm^2}$ were inferred from individual proton spectra measured from different lines of sight with wedge range filters [78]. Figure 26(b) shows the corresponding measured ρR as a function of CR and demonstrates that higher areal densities were achieved with increasing CR in SI implosions. Up to $\sim 35\%$ higher compression was achieved compared to implosions without the spike. These results again indicate that SI implosions with optimally timed pulse shapes show an improved performance, suggesting less instability growth.

It is not yet clear why the SI implosion perform much better than predicted, but there are several possible explanations. Large convergence ratios and the slow assembly make plastic shells inherently Rayleigh-Taylor instable during the deceleration phase. This gives rise to a substantial mixing of colder plastic shell material into the hot, compressed D_2 gas that quenches fusion reactions and generally results in a low YOC. Mixing is enhanced in these low-velocity implosions because the hot spot is small relative to the target size. The improved performance of SI implosions suggests that the mixing processes were mitigated for optimal shock-wave timing. This might be caused by the impulse acceleration by the spike shock wave shortening the time period for instability growth or by steepening of the density profile at the inner shell surface. It is interesting to note that simulations with spike pulses

[3, 54] predict the quenching of Rayleigh-Taylor growth by the spike, which was also measured in Rayleigh-Taylor experiments in the planar geometry [56].

So far, only a handful of cryogenic target 60-beam SI implosions were performed. The results are encouraging and the imploded shell reach close to the 1D predicted compression and the measured neutron yields were about 10% of the 1D predictions [57]. Unfortunately, symmetric 60-beam experiments on OMEGA with standard size targets only allow laser intensities of up to $\sim 0.8\,\mathrm{PW/cm^2}$ in the power spike, which is almost an order of magnitude lower than what is required [4]. The laser generated pressures are limited to $\sim 50\,\mathrm{Mbar}$ and are much weaker than the required 300 Mbar ablation pressure.

4.3.2. 40+20 beam implosions

In order to overcome the intensity limitation of standard 60-beam implosions, a new platform was developed that uses 40 beams with a low intensity to implode a capsule and the remaining 20 beams at a much higher intensity to interact with the converging shell later in time [34, 79]. Typical pulse shapes for the compression and spike beams are shown in figure 27(a). Different focusing options were tested for the spike beams allowing scanning of the single beam intensity from 0.5 up to $8\,\mathrm{PW/cm^2}$. The hydrodynamic performance of plastic shells filled with deuterium gas was studied both in experiments and in 2D hydrodynamic simulations. The experiments indicate a significant energy coupling by the high intensity spike beams into the capsule that is partially driven by a hot electron component of a moderate temperature of $\sim 30\,\mathrm{keV}$ and an increased thermal component.

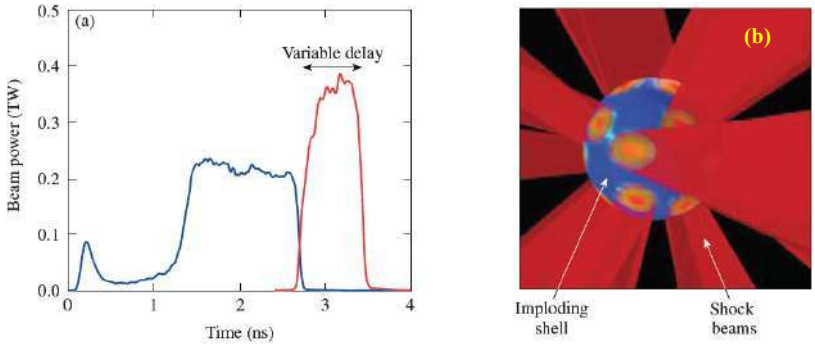

Figure 27. (Color online) a) The drive-pulse shape (blue) for the 40 beams and the high-intensity pulse (red) for the 20 spike beams. b) Schematics of the 20 delayed spike beams tightly focused onto the critical-density surface.

The experimental observables indicate that the hot electrons are primarily generated by SRS. The new platform also enables backscatter measurements at single-beam intensities of up $8\,\mathrm{PW/cm^2}$. Total reflectivity of up to 36% was measured, see figure 21 in Sec. 4.2.2 and the light is primarily scattered back into the high intensity beam without significant side scattering.

Hydrodynamic simulations with the 2D DRACO code [53] show the formation of a channel by a tightly focused single high intensity beam. This channel might be responsible for collimating most of the scattered light back into the focusing lens. The suppression of TPD was observed with increasing laser intensity and a decreasing

blue shift of the SBS signal, which is attributed to that the SBS activity shifts to higher plasma densities with increasing spike intensity. At the highest intensity, SBS from around the quarter critical density was measured. The interaction of driven ion acoustic and electron plasma waves at around quarter critical density might play a role in the suppression of TPD.

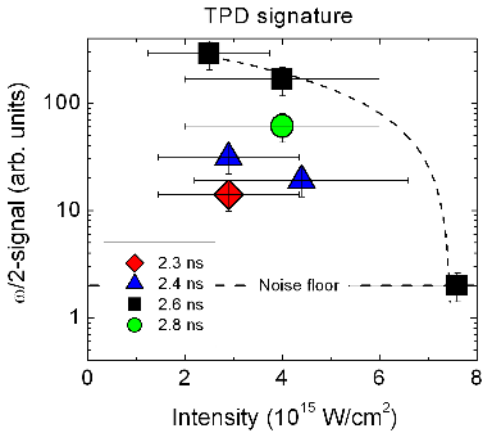

Figure 28. (Color online) Measured $\omega/2$ signal for various spike intensities and different spike onset times.

With increasing intensity, a strong reduction of the optical emission at the half-harmonic, $\omega/2$, of the laser frequency was observed, see figure 28. The $\omega/2$ signal decreased by more than two orders of magnitude in the experimental intensity range. At the maximum intensity, the $\omega/2$ signal was below the detection threshold, indicating no significant contribution of TPD to the hot-electron production. This and the relatively low hot-electron temperature of $\sim 30\,\mathrm{keV}$ supports the conjecture that SRS plays the dominant role in hot electron production in these experiments. The strong reduction of $\omega/2$ with intensity, together with the observed shift of the SBS active region to quarter critical density might indicate that driven ion acoustic waves play a role in the reduction of TPD. Most of the experiments were performed without phase plates in the spike beams and this makes the spike beams vulnerable to filamentation instabilities that probably disrupted the beams. The 20 spike beams were equipped in a few shots with small-spot phase plates. Encouraging results were obtained, indicating an enhanced coupling despite that a slightly hotter electron population was generated.

Important information was obtained from neutron yield measurements in the 40+20 experiments. It was found that the neutron yield enhancement when adding the 20 spike beams was independent of the single beam spike intensity. Figure 29(a) shows that adding the 20 spike beams, and therefore more energy on target, enhances the yield by a factor of up to 2.3, with a trend of slightly lower yields at later spike onset. The neutron yield shows no significant dependence on the spike intensity. A similar trend is observed in the predicted neutron yield from 1D simulations. There the enhancement is up to a factor of ~ 3.5 when adding the spike beams, slightly more than what was measured. A possible explanation why the yield increase is less than predicted might be that the 20 spike beams slightly increased illumination non-uniformities. The YOC was varied from 3 to 5% for these experiments. 2D CHIC [17]

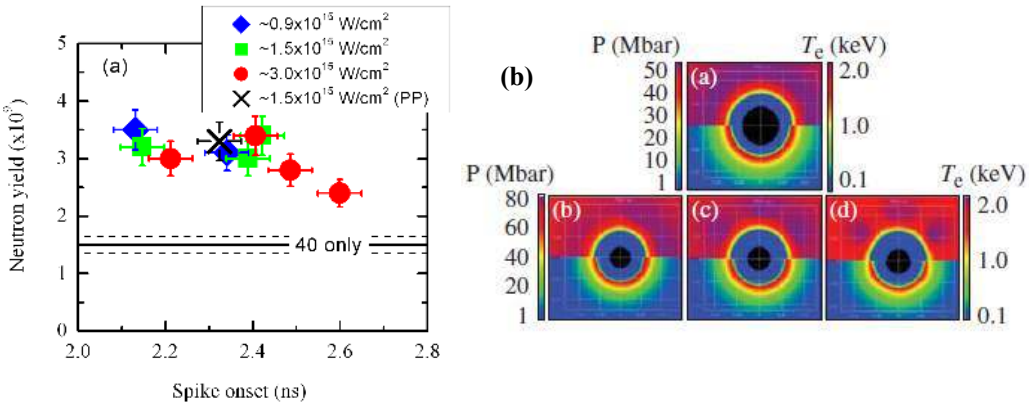

Figure 29. (Color online) a) Measured neutron yield for various spike onset times and spike intensities. (b) Two-dimensional CHIC simulations for different spike intensities. Electron temperature (top half) and pressure (bottom half) [34]. Reproduced with kind permission of the American Institute of Physics.

simulations show that even if some spike laser imprint in the corona is observed at high intensity, the pressure remains fairly symmetric, independently of the spike intensity on target. Figure 29(b) shows electron temperature (top half) and pressure (bottom half) maps obtained from various 2D simulations. Hot electrons were not included in the simulations. Independent of the spike intensity on target the pressure remains symmetric with the same value of ~ 75 Mbar. Some slight pressure modulations are observed at the highest intensity. The simulations show that the temperature in the conduction layer is fairly symmetric, which explains why the spike pressure keeps the same values in all the cases and as a consequence also the neutron yield. The neutron measurement therefore might be an indication of a mechanism that provides rapid isotropic heat dissipation in the conduction layer of the plasma (so called cloudy-day model) that was introduced in Sec. 3.3.1.

5. Conclusion

The shock ignition scheme has a relatively short history of about five years of intense studies. Although serious issues related to laser plasma interaction, energy transport and target hydrodynamics need further investigations, non of them can be considered as a show stopper. The major feature of SI combining the idea of separation of the implosion and ignition processes with a relatively low (sub-petawatt) ignition power makes it very attractive for direct testing on the major high energy laser installations NIF and LMJ. Although many problems remain to be solved, they are clearly identified.

The laser plasma interaction is the major unresolved point in the SI scheme. The existing multi-kilojoule laser installations except NIF and LMJ cannot provide at the same time the needed laser intensity and the spot size. So, the possibility to realize the ablation pressure in the 300 Mbar range is not yet demonstrated. The experiments with laser intensities exceeding the level of 1 PW/cm^2 are made with too small focal spots, with a size that is comparable to the distance between the absorption and ablation zones. Thus the absorbed energy flux was not transported to the shock

formation region.

Nevertheless, several encouraging results have been demonstrated. The OMEGA implosions in the spherical geometry show a clear improvement of the shell convergence ratio and the target areal density. The experimental results with warm shells are exceeding the theoretical expectations. Further experiments with the cryogenic targets will provide more information about the shock wave propagation and its effect on the compressed core.

The parametric instabilities in plasma corona remain the important issue. The observed SBS and SRS reflectivities in many experiments are in the range of tens of percent, which are comparable or below the theoretical estimates and numerical simulations. However, some experiments show higher reflectivity levels and production of energetic electrons. The simulations show the TPD instability near the quarter critical density suppressed in the competition with the SRS, and this effect is corroborated in the OMEGA experiments. The methods of spatial and temporal laser beam smoothing are not yet studied for the shock ignition conditions. They can be applied in future experiments on the installations with higher laser energy. The hot electrons with energies in the range below 100 keV should not penetrate the shell, but they may contribute to creation of a stronger ablation pressure. This issue of the hot electron transport needs further studies.

Awaiting first results of the integrated experiments on the NIF and LMJ in coming years, the studies of physical processes in the shock ignition scheme are in progress. Tight connections between the experiments, numerical simulations and theoretical developments provide an excellent opportunity for better comprehension and control of such crucial issues as laser coupling efficiency, hot electron transport, ablation pressure generation and stability of shell implosion.

Acknowledgments

The authors acknowledge the fruitful collaboration and discussion with all colleagues who contribute to the studies presented in this review. This work was performed within the framework of the HiPER project EC FP7, project no. 211737. It is partly supported by the EURATOM within the "Keep-in-Touch" activities and the Aquitaine Regional Council. The work on OMEGA was supported by the U.S. Department of Energy, Office of Fusion Energy Sciences under Contracts DE-FC02-04ER54789 and DE-FC52-08NA28302. The support to O.K. by the Czech Science Foundation, project P205/11/P660 is acknowledged. 1D PIC simulations were calculated on the HPC resources of CINES under the allocation 2012-056129 made by GENCI.

References

[1] Shcherbakov V.A. 1983 *Sov. Journ. Plasma Phys.* **9** 240
[2] Betti R. et al 2007 *Phys. Rev. Lett.* **98** 155001
[3] Ribeyre X. et al 2009 *Plasma Phys. Control. Fusion* **51** 015013
[4] Perkins L.J. et al 2009 *Phys. Rev. Lett.* **103** 045004
[5] Canaud B. and Temporal M. 2010 *New Journ. Phys.* **12** 043037
[6] Schmitt A.J. et al 2010 *Phys. Plasmas* **17** 042701
[7] Atzeni S. et al 2013 *Nuclear Fusion* **XX** XXXXXX
[8] Fabbro R., Max C. and Fabre E. 1985 *Phys. Fluids* **28** 1463
[9] Lindl J. 1995 *Phys. Plasmas* **2** 3933
[10] Atzeni S. and Meyer-ter-Vehn J. 2004 *The physics of inertial fusion* (Oxford: Clarendon Press)
[11] Moses E.I. and Wuest C.R. 2005 *Fusion Sci. Technol.* **47** 314

[12] Ebrardt J. and Chaput J.M. 2010 *J. Phys.: Conf. Ser.* **244** 032017
[13] Garban-Labaune C et al 1982 *Phys. Rev. Lett.* **48** 1018
[14] Drake R.P. et al 1984 *Phys. Rev. Lett.* **53** 1739
[15] Solodov A. A. and Betti R. 2008 *Phys. Plasmas* **15** 042707
[16] Skupsky S. et al 2004 *Phys. Plasmas* **11** 2763
[17] Maire P.H., Abgrall R., Breil J., and Ovadia J. 2007 SIAM J. Sci. Comput. **29**, 1781
[18] Kruer W. 1988 *The Physics of Laser Plasma Interactions* (New York: Addison-Wesley)
[19] Emery M.H. et al 1982 *Phys. Rev. Lett.* **48** 253; Kato Y. et al 1984 *ibid* **53** 1057
[20] Lushnikov P.M. and Rose H.A. 2006 *Plasma Phys. Control. Fusion* **48** 1501
[21] Grech M. et al 2009 *Phys. Rev. Lett.* **102** 155001
[22] Skupsky S. and Craxton R. S. 1999 *Phys. Plasmas* **6** 2157
[23] Vu H., DuBois D. and Bezzerides B. 2001 *Phys. Rev. Lett.* **86** 4306; 2002 *Phys. Plasmas* **9** 1745
[24] Liu C.S. and Rosenbluth M.N. 1976 *Phys. Fluids* **19** 967
[25] Simon A. et al 1983 *Phys. Fluids* **26** 3107
[26] Menyuk C.R. et al 1985 *Phys. Fluids* **28** 3409
[27] Afeyan B. and Williams E. 1995 *Phys. Rev. Lett.* **75** 4218
[28] Afeyan B. and Williams E. 1997 *Phys. Plasmas* **4** 3845
[29] Weber S. et al 2012 *Phys. Rev. E* **85** 016403
[30] Yan R. et al 2012 *Phys. Rev. Lett.* **108** 175002
[31] Regan S.P. et al 2010 *Phys. Plasmas* **17** 020703
[32] Klimo O. et al 2010 *Plasma Phys. Control. Fusion* **52** 055013
[33] Klimo O. et al 2011 *Phys. Plasmas* **18** 082709
[34] Theobald W. et al 2012 *Phys. Plasmas* **19** 102706
[35] Weber S., Riconda C. and Tikhonchuk V.T. 2005 *Phys. Rev. Lett.* **94** 055005
[36] Riconda C. et al 2011 *Phys. Plasmas* **18** 092701
[37] Code developed by A. Heŕon and J.-C. Adam at École Polytechnique, France
[38] Yin L. et al 2012 *Phys. Plasmas* **19** 056304
[39] Yin L. et al 2012 *Phys. Rev. Lett.* **108** 245004
[40] Malone R.C., McCrory R.L. and Morse R.L. 1975 *Phys. Rev. Lett.* **34** 721
[41] Spitzer L., Härm R. 1962 *Phys. Rev.* **89** 977
[42] McCall G.H. et al 1983 *Plasma Phys.* **25** 237
[43] Tan T.H. et al 1983 *Phys. Fluids* **24** 754
[44] Volosevich P.P., Rozanov V.B. 1981 *JETP Lett.* **33** 17
[45] Gus'kov S.Yu. et al 1983 *Sov. J. Quantum Electronics* **13** 498
[46] Evans R.G. 1983 *Laser & Part. Beams* **1** 231
[47] Evans R.G. 1986 *Plasma Phys. Control. Fusion* **28** 157
[48] Betti R. et al. 2007 *J. Phys.: Conf. Ser.* **112** 022024
[49] Bell A.R., Tzoufras M. 2011 *Plasma Phys. Control. Fusion* **53**, 045001
[50] Guskov S. et al. 2012 *Phys. Rev. Lett.* submitted
[51] Zhou C.D. and Betti R. 2007 *Phys. Plasmas* **14** 072703
[52] Ribeyre X. et al 2011 *Phys. Plasmas* **18** 102702
[53] Radha P.B. et al 2005 *Phys. Plasmas* **12** 032702
[54] Atzeni S., Schiavi A. and Marocchino A. 2011 *Plasma Phys. Control. Fusion* **53** 035010
[55] Hallo L. et al 2009 *Plasma Phys. Control. Fusion* **51** 014001
[56] Aglitskiy Y. et al 2009 *Phys. Rev. Lett.* **103** 085002
[57] Theobald W. et al 2008 *Phys. Plasmas* **15** 055503
[58] di Nicola J.-M. et al 2006 *J. Phys.* IV (France) **133** 595
[59] Depierreux S. et al 2009 *Phys. Rev. Lett.* **102** 195005
[60] Moody J.D. et al. 1996 *Phys. Rev. Lett.* **77** 1294
[61] Labaune C.. et al 2006 *Journal of Physics* IV **133** 29; Depierreux S. et al *ibid.* 317
[62] Depierreux S. at al 2012 *Phys. Plasmas* **19** 012705
[63] Labaune C. et al 2006 *Journal of Physics* IV **133** 29
[64] Baldis H.A. et al 1998 *Phys. Rev. Lett.* **80** 1900
[65] Drake R.P. et al 1996 *Phys. Rev. Lett.* **77** 79
[66] Fernandez J. et al 1998 *Phys. Rev. Lett.* **81** 2252
[67] Baldis H.A. et al 1996 *Phys. Rev. Lett.* **77** 2957
[68] Michel D.T. et al 2010 *Phys. Rev. Lett.* **104** 255001
[69] Baton S.D. et al 2012 *Phys. Rev. Lett.* **108** 195002
[70] Antonelli L. el al 2011 *Acta Tecnica* **56** T57
[71] Batani D. et al. 2011 *Plasma Phys. Control. Fusion* **53** 124041
[72] Hohenberger M. et al "Shock Ignition Experiments with Planar Targets on OMEGA" *Phys.*

Rev. Lett. submitted
[73] Smid M, Antonelli L., Renner O. 2012 "X-ray spectroscopic characterization of shock-ignition-relevant plasmas" *Acta Polytechnica* accepted
[74] Nejdl J. et al 2010 *Phys. Plasmas* **17** 122705
[75] See National Technical Information Service Document No. DE94011699 ("SESAME database" by J.D. Johnson, Los Alamos National Laboratory Report No. LA-UR-94-1451, 1994). Copies may be ordered from the National Technical Information Service, Springfield, VA 22161
[76] Perkins L.J. et al 2010 "On the Fielding of a High Gain, Shock-Ignited Target on the National Ignition Facility in the Near Term", Lawrence Livermore National Laboratory Technical Report, LLNL-TR-428513
[77] Craxton R.S. et al 2010 *Bull. Am. Phys. Soc.* **55** 26
[78] F. Seguin F. et al 2003 *Rev. Sci. Instrum.* **74** 975
[79] Theobald W. et al 2009 *Plasma Phys. Control. Fusion* **51** 124052